การตรวจสอบความถูกต้องของปริมาณรังสีในลำแสงโฟตอนสำหรับอะคูลอสเอกซ์บีอัลกอริทึม

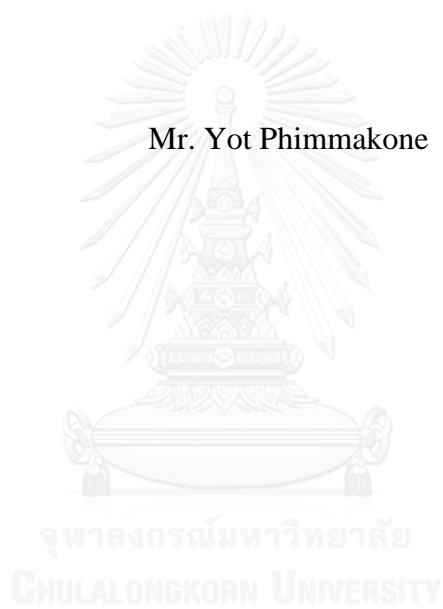นายยอด พิมมะกอน

วิทยานิพนธ์นี้เป็นส่วนหนึ่งของการศึกษาตามหลักสูตรปริญญาวิทยาศาสตรมหาบัณฑิต
สาขาวิชาฉายาเวชศาสตร์ ภาควิชารังสีวิทยา
คณะแพทยศาสตร์ จุฬาลงกรณ์มหาวิทยาลัย
ปีการศึกษา 2559
ลิขสิทธิ์ของจุฬาลงกรณ์มหาวิทยาลัย

DOSIMETRIC VERIFICATION IN PHOTON BEAMS FOR ACUROS XB
ALGORITHM

Mr. Yot Phimmakone

A Thesis Submitted in Partial Fulfillment of the Requirements
for the Degree of Master of Science Program in Medical Imaging
Department of Radiology
Faculty of Medicine
Chulalongkorn University
Academic Year 2016

Thesis Title	DOSIMETRIC VERIFICATION IN PHOTON BEAMS FOR ACUROS XB ALGORITHM
By	Mr. Yot Phimmakone
Field of Study	Medical Imaging
Thesis Advisor	Associate Professor Sivalee Suriyapee, M. Eng.
Thesis Co-Advisor	Taweap Sanghangthum, Ph.D.

Accepted by the Faculty of Medicine, Chulalongkorn University in Partial Fulfillment of the Requirements for the Master's Degree

.... Dean of the Faculty of Medicine

(Professor Suttipong Wacharasindhu, M.D.)

THESIS COMMITTEE

.... Chairman

(Chakkapong Chakkabat, M.D.)

.... Thesis Advisor

(Associate Professor Sivalee Suriyapee, M. Eng.)

.... Thesis Co-Advisor

(Taweap Sanghangthum, Ph.D.)

.... External Examiner

(Professor Franco Milano, Ph.D.)

ยอด พิมมะกอน : การตรวจสอบความถูกต้องของปริมาณรังสีในลำแสงโฟตอนสำหรับอะคูลอสเอกซ์บีอัลกอริทึม (DOSIMETRIC VERIFICATION IN PHOTON BEAMS FOR ACUROS XB ALGORITHM) อ.ที่ปรึกษาวิทยานิพนธ์หลัก: รศ.ศิวลี สุริยาปี, อ.ที่ปรึกษาวิทยานิพนธ์ร่วม: ดร.ทวีป แสงแห่งธรรม, 63 หน้า.

วัตถุประสงค์ของงานวิจัยนี้เพื่อตรวจสอบความถูกต้องของโปรแกรมวางแผนการรักษา Eclipse ที่ใช้อะคูลอสเอกซ์บีอัลกอริทึมคำนวณปริมาณรังสีของรังสีเอกซ์ 6 MV โดยการเปรียบเทียบคุณลักษณะเฉพาะและการนำไปใช้งานทางคลินิกกับการวัดจริง ทำการเปรียบเทียบคุณลักษณะเฉพาะของลำรังสีชนิดสี่เหลี่ยมจัตุรัสและผืนผ้า ด้วยการพิจารณาปริมาณรังสีตามความลึก และพิจารณาปริมาณรังสีทางด้านข้างที่ความลึกต่างๆ วัดปริมาณรังสีตามความลึกด้วยแชมเบอร์รุ่น CC13 วัดปริมาณรังสีทางด้านข้างที่ความลึก 5, 10 และ 20 ซม ด้วยไดโอด PFD ส่วนสัดส่วนเอาท์พุทที่ความลึก 10 ซม ใช้วัดด้วยแชมเบอร์รุ่น CC13 สำหรับการประยุกต์ใช้ทางคลินิก ทำการเลือกแผนการรักษาบริเวณศีรษะ ทรวงอก และอุ้งเชิงกราน ในเทคนิคการรักษาแบบสามมิติ แบบปรับความเข้ม และแบบปรับความเข้มชนิดหัวเครื่องหมุนรอบตัวผู้ป่วย อย่างละ 15 แผนการรักษา ศึกษาทั้งในแฟนทอมเนื้อเดียวและแฟนทอมที่มีความแตกต่างของเนื้อเยื่อ โดยวัดรังสีเป็นจุดด้วยแชมเบอร์รุ่น CC13 และเปรียบเทียบกับค่าที่คำนวณได้จาก Eclipse ผลการทดลองพบว่าปริมาณรังสีในแนวความลึกที่วัดได้มีความใกล้เคียงกับที่ได้จากการคำนวณ โดยค่าเฉลี่ยของ δ_1 (ปริมาณรังสีสูงและความชันของปริมาณรังสีน้อย) อยู่ที่ 0.16±0.64% และค่า δ_2 (ปริมาณรังสีสูงและความชันของปริมาณรังสีมาก) อยู่ที่ 0.43±0.70 มม. ในส่วนปริมาณรังสีในแนวด้านข้างทั้ง in-plane และ cross-plane ในทุกขนาดลำรังสีและทุกความลึก พบว่าค่า δ_2 อยู่ภายใน 2 มม ค่า δ_3 (ปริมาณรังสีสูงและความชันของปริมาณรังสีน้อย) อยู่ภายใน 3% ค่า δ_4 (ปริมาณรังสีต่ำและความชันของปริมาณรังสีน้อย) อยู่ภายใน 3% และ δ_{50-90} อยู่ภายใน 2 มม ค่าสัดส่วนเอาท์พุทพบความแตกต่างสูงสุดอยู่ที่ -1.54% ในส่วนของการประยุกต์ใช้ในทางคลินิก ผลการตรวจสอบปริมาณรังสีในแฟนทอมเนื้อเดียวพบความแตกต่างสูงสุดในเทคนิคการรักษาแบบ 3 มิติที่ 0.71% สำหรับแผนการรักษาแบบปรับความเข้มที่ -2.95% และ สำหรับแผนการรักษาแบบปรับความเข้มชนิดหัวเครื่องหมุนรอบตัวที่ 2.70% ขณะที่ในแฟนทอมที่มีความแตกต่างของเนื้อเยื่อ พบความแตกต่างในเทคนิค 3 มิติ เทคนิคปรับความเข้ม และเทคนิคปรับความเข้มแบบหัวเครื่องหมุนรอบตัวอยู่ที่ 0.61%, -2.27% และ -1.9% ตามลำดับ ซึ่งความแตกต่างเหล่านี้อยู่ภายในขีดจำกัดการยอมรับที่ ±3% สำหรับแฟนทอมเนื้อเดียว และ ±5% สำหรับแฟนทอมที่มีความแตกต่างของเนื้อเยื่อ ตามมาตรฐาน AAPM TG-53 และ IAEA TRS 430 ดังนั้นจึงสรุปได้ว่าอะคูลอสเอกซ์บีอัลกอริทึม ในเครื่องวางแผนการรักษา Eclipse สามารถนำมาใช้ในการวางแผนการรักษาผู้ป่วยได้อย่างถูกต้อง.

ภาควิชา	รังสีวิทยา	ลายมือชื่อนิสิต	....
สาขาวิชา	ฉายาเวชศาสตร์	ลายมือชื่อ อ.ที่ปรึกษาหลัก	....
ปีการศึกษา	2559	ลายมือชื่อ อ.ที่ปรึกษาร่วม	....

5874101030 : MAJOR MEDICAL IMAGING

KEYWORDS: ACUROS XB ALGORITHM / DOSE VERIFICATION / 3D-CRT, IMRT, VMAT

YOT PHIMMAKONE: DOSIMETRIC VERIFICATION IN PHOTON BEAMS FOR ACUROS XB ALGORITHM. ADVISOR: ASSOC. PROF. SIVALEE SURIYAPEE, M. Eng., CO-ADVISOR: TAWEAP SANGHANGTHUM, Ph.D., 63 pp.

The purpose of this study is to verify dosimetric accuracy of 6 MV X-ray beams for Acuros XB algorithm in Eclipse TPS by comparing measurements and calculations of beam characteristics and clinical applications. The beam characteristics were studied in various square and rectangular fields for PDDs, profiles and output factors by measurement in water phantom. The PDDs were measured by scanning with CC13 ion chamber, while in-plane and cross-plane profiles were acquired with PFD diode at 5, 10 and 20 cm depths. The output factors were measured at 10 cm depth using CC13 ion chamber. In clinical applications, the selected 15 cases in head, chest and pelvic regions of 3D-CRT, IMRT and VMAT techniques in homogeneous and heterogeneous medium were measured with CC13 ion chamber and compared with calculated dose in Eclipse TPS. The results of measured PDDs showed a good agreement to TPS with the average of δ_1 (high dose, small dose gradient) at 0.16±0.64% and δ_2 (high dose, large dose gradient) at 0.43±0.70 mm. Both measured in-plane and cross-plan profiles in all field sizes and all depths displayed the coincidence results with calculated profiles that showed δ_2 less than 2 mm, δ_3 (high dose, small dose gradient) within 3%, δ_4 (low dose, small dose gradient) within 3%, and δ_{50-90} within 2 mm. The maximum output factors differences were -1.54%. For clinical application, the dose verification in homogeneous showed the maximum dose differences of 0.71% for 3D-CRT, -2.95% for IMRT and 2.70% for VMAT plans. While, inhomogeneous showed of the maximum dose error of 3D-CRT, IMRT, and VMAT plans at 0.61%, -2.27%, and -1.9% for 3D-CRT, IMRT, and VMAT plans, respectively. These dose differences were within the tolerance of ±3% for homogeneous and ±5% for heterogeneous medium as the recommendation from AAPM TG-53 and IAEA TRS 430. Therefore, the Acuros XB algorithm can be implemented in Eclipse TPS of clinical application radiotherapy.

Department:	Radiology	Student's Signature	....
Field of Study:	Medical Imaging	Advisor's Signature	....
Academic Year:	2016	Co-Advisor's Signature	....

ACKNOWLEDGEMENTS

CONTENTS

LIST OF TABLES

LIST OF FIGURES

LIST OF ABBREVIATIONS

ABBREVIATION	TERMS
AAPM	American Association of Physicist in Medicine
AAA	Anisotropic Analytical Algorithm
AXB	Acuros XB
BP	Beam Profile
CSD	Continuous Slowing Down
CV	Coefficient of variation
CT	Computed Tomography
CU	Calibrated Unit
CIRS	Computerized Imaging Reference Systems
DTA	Distance to Agreement
EPID	Electronic Portal Imaging Device
FS	Field Size
FFF	Flattening Filter Free
IAEA	International Atomic Energy Agency
IMRT	Intensity Modulated Radiation Therapy
ICRU	Internal Commission on Radiation Units
IGRT	Image Guided Radiation Therapy
IC	Ionization Chamber
LBTE	Linear Boltzmann Transport Equation
MLC	Multileaf-Collimator
MRI	Magnetic Resonance Imaging
OF	Output Factor
PDD	Percentage Depth Dose
PET	Positron Emission Tomography
PTV	Planning Target Volume
QA	Quality Assurance
SDD	Source to Detector Distance
SSD	Source to Surface Distance
SAD	Source to Axis Distance
SD	Standard Deviation
SBRT	Stereotactic Body Radiotherapy
TPS	Treatment Planning System
TG	Trask Group
TLD	Thermo-luminescent Dosimeter
VMAT	Volumetric Modulated Arc Therapy
2D	Two Dimensional
3DCRT	Three-Dimensional Conformal Radiotherapy
MV	Megavoltage
MU	Monitor Unit
MeV	Mega Electron Volt
kVp	Kilo Volt Peak
keV	Kilo Electron Volt

ABBREVIATION	TERMS
K_{TP}	Correction Factor for Temperature and Pressure
K_s	Correction Factor for Ion Recombination
K_Q	Correction Factor for Temperature and Pressure
kPa	Kilopascal
$N_{D,W}$	Calibration Factor in Terms of Absorbed Dose to Water
cGy	Centigray
mSv	Millimeter Sievert
nC	Nano-Coulomb
mm^3	Cubic Millimeter
cm	Centimeter
cm^2	Centimeter Square
cm^3	Cubic Centimeter
R	Roentgen
Bq	Becquerel
Ci	Curie
T	Temperature
P	Pressure
A	Ampere
C	Coulomb
D_{max}	Maximum Dose
D_{mean}	Mean Dose
D_{do}	Dose at the Reference Depth
D_d	Dose at the any Depth
D_s	Dose at the Surface

จุฬาลงกรณ์มหาวิทยาลัย
CHULALONGKORN UNIVERSITY

CHAPTER I

INTRODUCTION

1.1 Background and Rationale

Radiation therapy is one of the most common treatment methods to treat cancer by delivering high radiation dose to the tumor while avoiding the normal tissues from receiving doses above their limitation. The development in dose photon calculation algorithm aims to increase the precision of radiation dose to tumor. The dose calculation algorithms have evolved significantly over the years from the simple calculations to the complex Monte Carlo calculation [1].

In 2010, Eclipse treatment planning system (Varian Medical Systems, Palo Alto, CA, USA) had introduced the new photon dose calculation algorithm called "Acuros XB". It was developed to administer accuracy and speed in external beam radiotherapy. Acuros XB algorithm is based on Linear Boltzmann Transport Equation (LBTE) [2]. The LBTE is the linearized form of the BTE, which assumes that radiation particles only interact with the matter they are passing through.

Acuros XB (external beam) was developed to provide the accuracy of Monte Carlo calculations while reducing the calculation time to an acceptable level. As an alternative to the statistical analysis done by Monte Carlo, Acuros XB solves the LBTE numerically. This technique removes errors from statistical noise common with Monte Carlo but instead introduces systematic errors. These errors are due to Acuros XB algorithm discretizing in space, angle and energy in the iteration process to reduce the calculation time. In addition, Acuros XB algorithm is considered to be similar to Monte Carlo methods due to the accurate modeling of dose deposition in heterogeneous media.

Several studies of Acuros XB algorithm validation have been conducted and showed comparable the results of dose calculation to Monte Carlo simulation in homogeneous and heterogeneous medium. However, previous observations did not evaluate Acuros XB algorithm calculation according to the American Association of Physicists in Medicine Task Group 53 (AAPM TG-53). AAPM TG-53 has been established in 1998 to guide and assist medical physicist who works in Radiotherapy field to develop and implement the comprehensiveness in QA radiotherapy treatment planning including software and algorithm in Radiotherapy Treatment Planning System [3].

This study aims to investigate the dosimetric accuracy of Acuros XB algorithms in percentage depth doses, beam profiles and output factors according to AAPM TG-53 protocol. Furthermore, this study would like to compare the dosimetric parameters between measurement and calculation in homogeneous and heterogeneous medium on three different techniques, 3D-CRT, IMRT and VMAT plans in head, chest and pelvic regions.

1.2 Research Objective

To investigate the dosimetric accuracy of Acuros XB algorithm implemented in Eclipse treatment planning system according to American Association of Physicist Medicine Task Group 53 (AAPM TG-53) and International Atomic Energy Agency Technical Reports Series 430 (IAEA TRS 430) protocols.

CHAPTER II

LITERATURE REVIEWS

2.1 Theories

2.1.1 Acuros XB Algorithm

Acuros XB (AXB) uses the same multiple source model as Anisotropic Analytical Algorithm (AAA) for primary beam, extra-focal beam and contaminant electron contributions. The Acuros XB algorithm calculation consists of four main steps which could be explained as follows [4]:

Step 1: Transport of source model fluence into the patient

The external photon and electron sources, q^γ and q^e, are modeled as anisotropic point sources in Acuros XB algorithm. At each static beam phase space (i.e control point), a separate point source exists for each of the AAA sources. For the primary source, the anisotropy of q^γ is described through a 2D fluence grid, in which both the particle fluence and energy spectra are spatially variable. For the extra-focal and wedge scatter source, the anisotropy of q^e is described through a 3D fluence grid and the energy spectra are spatially constant. For the electron contamination source, the anisotropy of q^e is described through a 3D fluence grid and the energy spectra are spatially constant. All point source is located at the target for the respective control point following equation (1) as follows:

$$\widehat{\Omega} \cdot \vec{\nabla}\Psi^\gamma + \sigma_t^\gamma \Psi^\gamma = q^{\gamma\gamma} + q^\gamma \tag{1}$$

$$\widehat{\Omega} \cdot \vec{\nabla}\Psi^\gamma + \sigma_t^\gamma \Psi^\gamma = q^{\gamma\gamma} + q^\gamma(E,\widehat{\Omega})\delta(\vec{r} - \vec{r}_p) \tag{2}$$

Where, Ψ^γ = Angular photon energy fluence or fluence if not time integrated, $\Psi^\gamma(\vec{r}, E, \widehat{\Omega})$ as a function of position, $\vec{r} = (x, y, z)$ and $\widehat{\Omega} = (\mu, \eta, \zeta)$

Ψ^e = Angular electron fluence, $\Psi^e(\vec{r}, E, \widehat{\Omega})$

$q^{\gamma\gamma}$ = Photon-to-photon scattering source, $q^{\gamma\gamma}(\vec{r}, E, \widehat{\Omega})$, which is the photon source resulting from photon interactions

q^γ = Extraneous photon source, $q^\gamma(E, \widehat{\Omega})$ for point source P, at position $\vec{r}_p$

σ_t^γ = Microscopic photon total cross section, $\sigma_t^\gamma(\vec{r}, E)$ and δ = Direct delta function

The principle of linear superposition may be used to define the photon angular fluence as the summation of un-collided and collided fluence components.

$$\Psi^\gamma \equiv \Psi^\gamma_{unc} + \Psi^\gamma_{coll} \tag{3}$$

Where, Ψ^γ_{unc} = Un-collided or un-scattered, photon angular fluence

Ψ^γ_{coll} = Collided or scatter, photon angular fluence

Substituting equation (3) into equation (2), leads to the following equation for the un-collided photon fluence:

$$\widehat{\Omega} \cdot \vec{\nabla}\Psi^\gamma_{unc} + \sigma^\gamma_t \Psi^\gamma_{unc} = q^\gamma(E, \widehat{\Omega})\delta(\vec{r} - \vec{r}_p) \tag{4}$$

A property of equation (4) is that Ψ^γ_{unc} can be solved analytically. Therefore, Ψ^γ_{unc} can be solved by using equation (5) below.

$$\Psi^\gamma_{unc}(\vec{r}, E, \widehat{\Omega}) = \delta(\widehat{\Omega} - \widehat{\Omega}_{\vec{r},\vec{r}_p}) \frac{q^\gamma(E,\widehat{\Omega})e^{-\tau(\vec{r},\vec{r}_p)}}{4\pi|\vec{r}-\vec{r}_p|^2} \tag{5}$$

Whereas, $\widehat{\Omega}_{\vec{r},\vec{r}_p} = \frac{\vec{r}-\vec{r}_p}{|\vec{r}-\vec{r}_p|}$, $\vec{r}$ and $\vec{r}_p$ are the source and destination point of the ray trace, respectively.

$\tau(\vec{r}, \vec{r}_p)$ = The optical distance (measured in mean free paths) between $\vec{r}$ and $\vec{r}_p$.

Equation (5) is solved for each primary, extra focal and wedge source in the calculation to compute Ψ^γ_{unc} throughout the patient. The electron contaminant source is modeled in a similar manner, but with the inclusion of the continuous slowing down (CSD) operator to account for charged particle interactions.

Step 2: Transport of scattered photon fluence in the patient

Once equation (5) is solved, $q^{\gamma\gamma}_{unc}$ is considered a fixed source in equation (6), which is solved to compute Ψ^γ_{coll} throughout the patient:

$$\widehat{\Omega} \cdot \vec{\nabla}\Psi^\gamma_{coll} + \sigma^\gamma_t \Psi^\gamma_{coll} = q^{\gamma\gamma}_{coll} + q^{\gamma\gamma}_{unc} \tag{6}$$

Step 3: Transport of scattered electron fluence in the patient

Once equation (6) is solved, $q_{coll}^{\gamma e}$ is considered a fixed source in equation (7). Similarly, from the solution to equation (5), $q_{unc}^{\gamma e}$ is also considered a fixed source. This equation (7) is solved to compute Ψ^e throughout the patient.

$$\widehat{\Omega} \cdot \vec{\nabla}\Psi^e + \sigma_t^e \Psi^e - \frac{\partial}{\partial E} S_R \Psi^e = q^{ee} + q_{coll}^{\gamma e} + q_{unc}^{\gamma e} + q^e \tag{7}$$

Where,

$q_{unc}^{\gamma\gamma}$ = First scattered photon source

$q_{coll}^{\gamma\gamma}$ = Secondary scattered photon source

S_R = Restricted collisional plus radiative stopping power, $S_R(\vec{r}, E)$

Step 4: Dose calculation

In the entire steps, the dose in any voxel is obtained through applying an energy dependent fluence to dose response function to the local energy dependent electron fluence in that voxel. The equation for dose calculation as follows:

$$D_i = \int_0^\infty dE \int_\Lambda d\widehat{\Omega} \frac{\sigma_{ED}^e(\vec{r}, E)}{\rho(\vec{r})} \psi^e(\vec{r}, E, \widehat{\Omega}) \tag{8}$$

Where,

D_i represents dose in any output grid voxel, i and σ_{ED}^e is macroscopic electron energy deposition cross sections in unit *MeV/cm*, $\rho(\vec{r})$ represents material density in the unit of *gr/cm³* and ψ^e is energy dependence of fluence.

As a contrary to AAA, which calculates each field separately, Acuros XB algorithm offers the choice of one calculation for the entire plan regardless of number of fields (plan sum). The drawback to this is that the dose is related to the whole plan and making changes to one field in a conventional plan, such as adjusting the field weight, cannot be accomplished. For a plan sum calculation, the ray-tracing step is the only step repeated for each field or beam angle while the time-consuming scatter calculations are done just once. This significantly reduces the time required for plans with number of fields, such as VMAT plans. Single fields, however, require longer calculation times than the identical AAA calculations [5].

2.1.2 Beam Characteristics

2.1.2.1 Percentage Depth Doses

As the photon beam is incident on a patient or phantom, the absorbed dose in the patient varies with depth. This variation depends on many conditions such as beam energy, depth, field size and distance from source and beam collimator system. Thus, the calculation of dose in the patient involves considerations in regarding to these parameters and other as they affect depth dose distribution. An essential step in the dose calculation system is to establish depth dose variation along the central axis the beam [6].

One way to characterize the central axis dose distribution is to normalize the dose at depth with respect to dose at a reference depth as expressed in equation (9) and shown in figure 2.1. This is called percentage depth dose that can be utilized to express the beam quality.
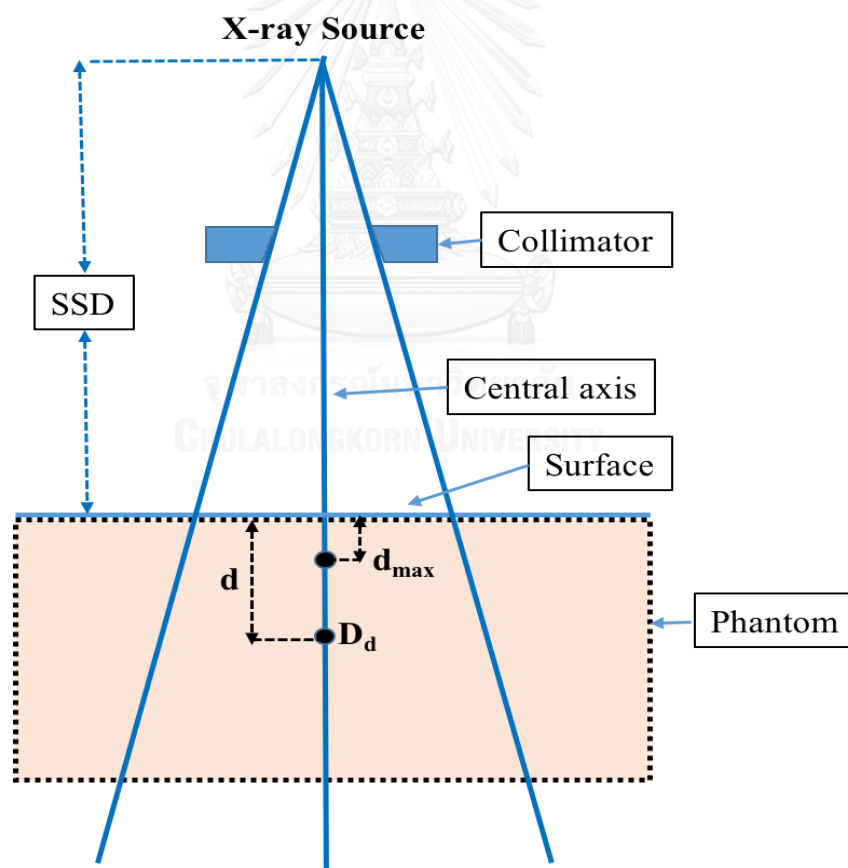
Figure 2.1 Percentage depth dose measured in water phantom

$$PDD = \frac{D_d}{D_{d_{max}}} \times 100 \tag{9}$$

Where,

d is any depth and d_0 is reference depth of maximum dose ($d_m=d_0$).

For orthovoltage (up to about 400 kVp) and lower-energy x-rays, the reference depth is usually the surface ($d_m=0$). For higher energies, the reference depth is taken at the position of the peak absorbed dose ($d_m= d_o$) [7].

To compare the percentage depth dose between measurements and calculations, parameters δ_1 and δ_2 could be used as shown in figure 2.2 according to American Association of Physicists in Medicine (AAPM TG-53) and IAEA TRS 430 [3, 8]. The parameters are shown below:

1. δ_1 is central beam axis for high dose and small gradient.
2. δ_2 is buildup region of central axis depth dose for high dose and large dose gradient.

The required tolerances for δ_1 of 2% and δ_2 of 2 mm were used in this research.
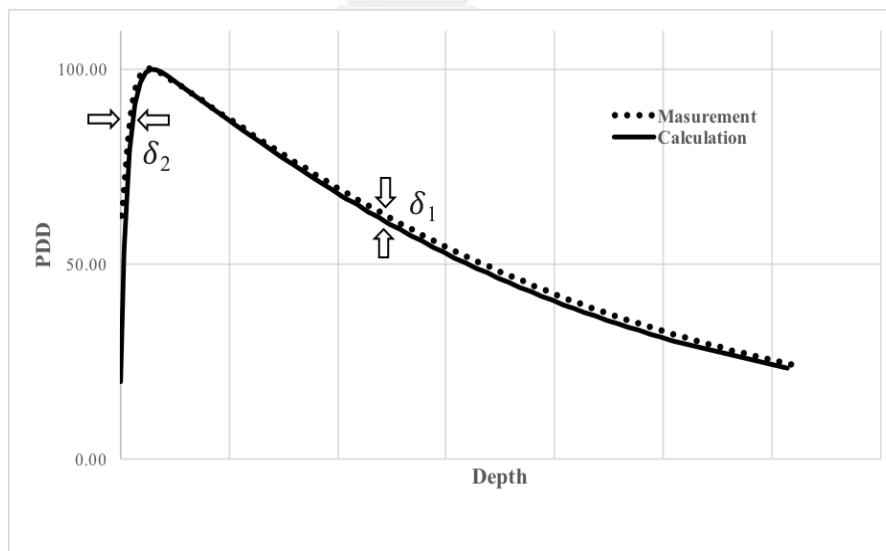
Figure 2.2 The parameters for percentage depth dose between measurement and calculation

2.1.2.2 Beam Profiles

Beam profiles represent percent dose in a plane perpendicular to the beam axis at a fixed depth. Figure 2.3, shows the way to scan beam profiles in water phantom.
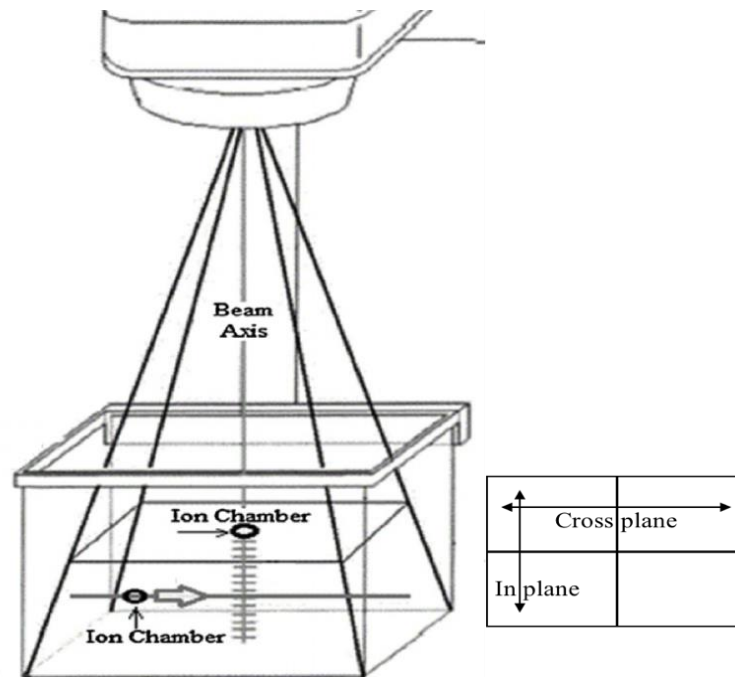
Figure 2.3 Beam profile measurement in-plane and cross-plane direction in water phantom

Such a representation of the beam is known as the beam profile for in-plane or cross-plane profiles. It may be noted that the field size is defined as the lateral distance between the 50% isodose lines at a reference depth. This definition is practically achieved by a procedure called the beam alignment in with the defining light is made to coincide with the 50% isodose lines of the radiation beam projected on a plane perpendicular to the beam axis and at the standard source to surface distance (SSD) or source to axis distance (SAD) [9]. The beam profile is used to explain beam flatness and symmetry.

To compare the beam profile between measurements and calculations according to AAPM TG-53 and IAEA TRS 430, the δ_2, δ_3, δ_4 and δ_{50-90} are the parameters representing the beam profile comparison which shown in figure 2.4, whereas:

1. δ_2 is penumbra region of profile for high dose and large dose gradient.
2. δ_3 is outside central beam axis for high dose and small dose gradient.
3. δ_4 is outside beam edges for low dose and small dose gradient.
4. δ_{50-90} is beam fringe for the distance between 50% to 90% dose.

The required tolerances 2 mm for δ_2, δ_{50-90} and 3% for δ_3, δ_4 were used in this research. The measurements are represented by solid lines while the calculation is represented by dotted lines [3].
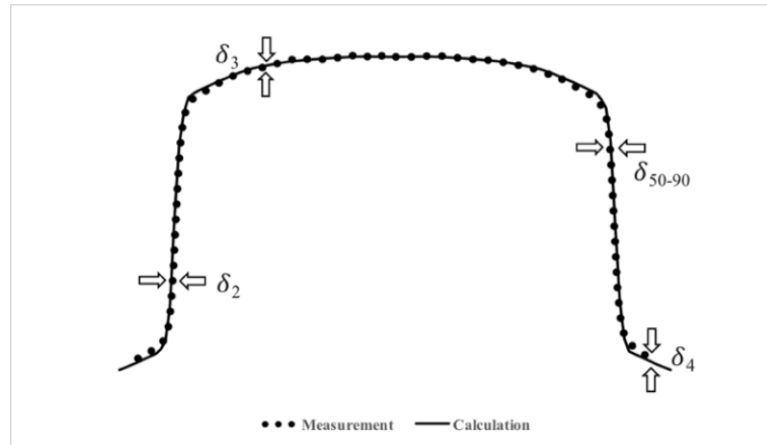
Figure 2.4 The parameters for beam profile between measurement and calculation

2.1.2.3 Output Factors

The output factor is defined as the ratio of the dose for any field size to the dose for a reference field at the same source to surface distance (SSD) and at the same depth in water phantom. Usually the reference field size is a square field of 10x10 cm^2 at maximum depth (d_{max}) of 1.5 cm for 6 MV photon beams or at the reference depth. The equation for output factor as follows (10) [10].

$$Output\ Factor = \frac{Output\ at\ any\ field\ size}{Output\ at\ reference\ field\ size\ (10x10\ cm^2)} \quad (10)$$

The output is an intrinsic characteristic of the accelerator and is measured periodically to make sure that the accelerator is operating properly in order to treat patients. As mentioned above, in radiation therapy, the output factor is measured in water phantom. However, for the purpose of verifying our detection system and its calibration, we also measured the dose given by various square fields and rectangular fields normalized to the reference field and we refer to it as output factor as well.

The accuracy of output factors calculations is an important feature of any treatment planning system. This study, output factors were measured for square field and rectangular field sizes. The accuracy of calculated output factors compared with measurement should be less than 2% [11].

2.1.3   Treatment Techniques

The treatment techniques in radiotherapy consist of: Three Dimensional Conformal Radiotherapy (3D-CRT), Intensity Modulated Radiation Therapy (IMRT) and Volumetric Modulated Arc Therapy (VMAT).

2.1.3.1 Three Dimensional Conformal Radiotherapy (3D-CRT)

Three dimensional, beam shaping and irradiation of tumors through multiple fields from different beam angles to reduce the dose to normal tissues have always been presented in radiotherapy practice. When the appropriate technology to deliver 3D-CRT, such as CT simulators, radiation treatment planning systems (RTPS) capable of performing three dimensional dose calculations, producing digitally reconstructed radiographs (DRRs) and DVHs and beam shaping devices such as multi-leaf collimators (MLCs) became available, this way of planning and delivering radiotherapy soon gained popularity. This has now become standard practice in the developed world when treating many types of tumors with curative intent.

The 3D-CRT technique allows physicians to give the high dose to tumor volume while sparing normal tissues. The 3D-CRT planning utilizes sophisticated computer technologies such as computed tomography (CT) scans, magnetic resonance imaging (MRI) and positron emission tomography (PET) images to view tumors in 3D-width, height and depth. With superior tumor imaging, patient treatment plans can be created with greater precision and accurately delineate target volume in computer based treatment planning system. 3D-CRT is now routinely used at most radiotherapy centers. The treatment plan of 3D-CRT technique is shown in figure 2.5 [12].
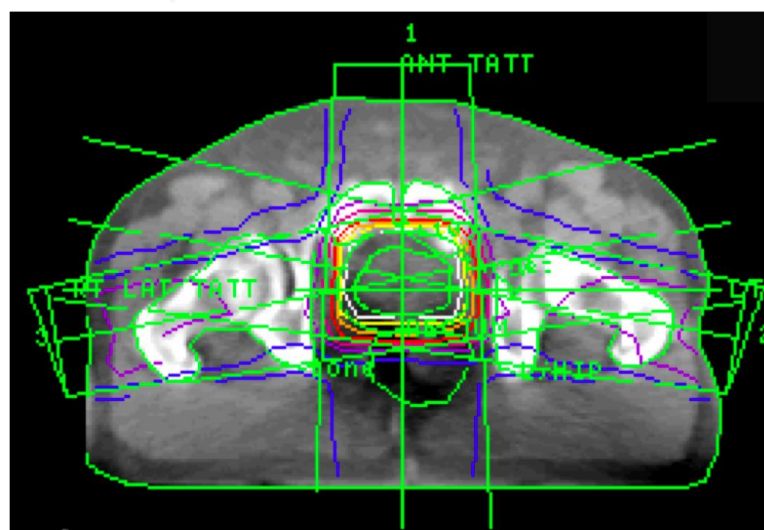
Figure 2.5 Three dimensional conformal radiotherapy technique

2.1.3.2 Intensity Modulated Radiation Therapy (IMRT)

The process of IMRT includes patient immobilization, 3D imaging, inverse planning, leaf sequencing, plan verification, patient setup verification, and treatment delivery. IMRT requires more stringent tolerance limits for patient immobilization than 3D-CRT. This is because IMRT treatment delivery may take a longer time, thus increasing the potential for intra-fraction patient motion. Moreover, the computer optimization process in inverse planning depends on the accurate delineation of target volume and critical structures, and their spatial integrity relative to each other [13].

IMRT is an advanced mode of high-precision radiation therapy treatment technique. It uses the advanced computer controlled linear accelerators machine to deliver highly precise and conformal radiation doses to tumor while move sparing the surrounding dose to normal tissues compared to 3D-CRT technique by modulating the beams using MLC movement. With the aids of 3D-CRT computed tomography (CT) or magnetic resonance imaging (MRI) for computerized dose calculations of IMRT plan, the best dose distribution pattern that is best conform to the tumor shape can be provided.

The most distinct feature of IMRT is the inverse planning. It specifies the plan outcome in terms of the tumor dose and normal structure dose limits and then the computer system adjusts the beam intensities to find a configuration best matched to the desired plan. An IMRT plan consists of several beams with the number of 5 or 7 or 9 beams as shown in figure 2.6. The use of several beams can build up a highly conformal dose distribution, allowing precise shape to a curved target and thus further spare of normal tissues. Each beam is subdivided into hundreds of beams lets and each beam let has an individual intensity [14].
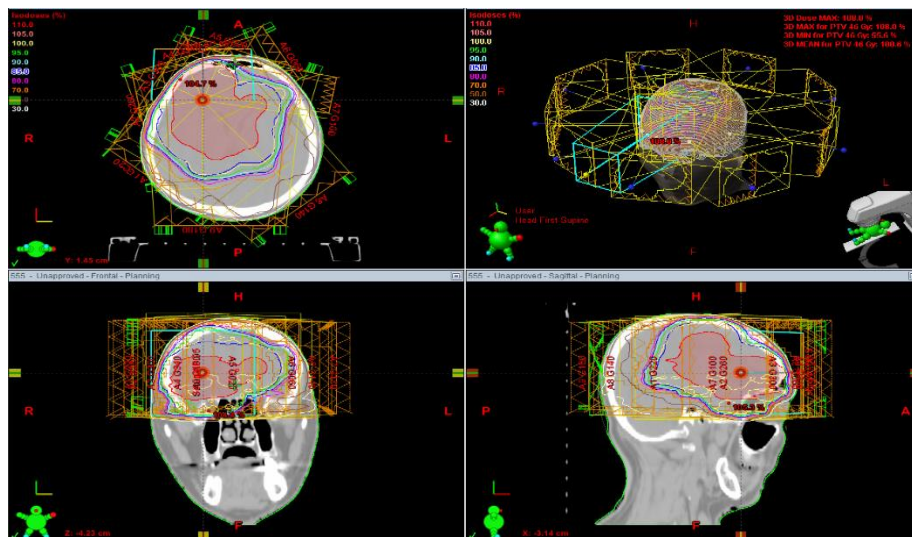
Figure 2.6 Intensity modulated radiation therapy technique

2.1.3.3 Volumetric Modulated Arc Therapy (VMAT)

The volumetric modulated arc therapy (VMAT) technique is an extension of IMRT. Instead of using number of static fields, one lets the gantry rotate during beam on time. The gantry rotation speed, dose rate and the position of the MLC leaflets change continuously during the treatment. Compared to IMRT, a VMAT plan delivers less monitor unit (MU) and less secondary dose to the normal tissues. In the clinic, VMAT is beneficial in treating head and neck as well as pelvic tumors due to a reduction in organ as risk toxicity compared to conventional plans [15].

The setup of an IMRT or VMAT plan in the treatment planning system is called in-verse planning. First, in-verse planning will specify dose constraint as well as the Dose Volume Histogram (DVH). Second, the treatment planning system will optimize the fields or arc to fit these criteria by running an iterative minimizing algorithm. A full dose calculation is done after. When calculating a VMAT plan the arc is split into discrete arc segments which functions as fields for the dose calculation [16]. Although taking less time to treat, VMAT plans take more time to calculate in the treatment planning process and the treatment plan of VMAT technique is shown in figure 2.7.
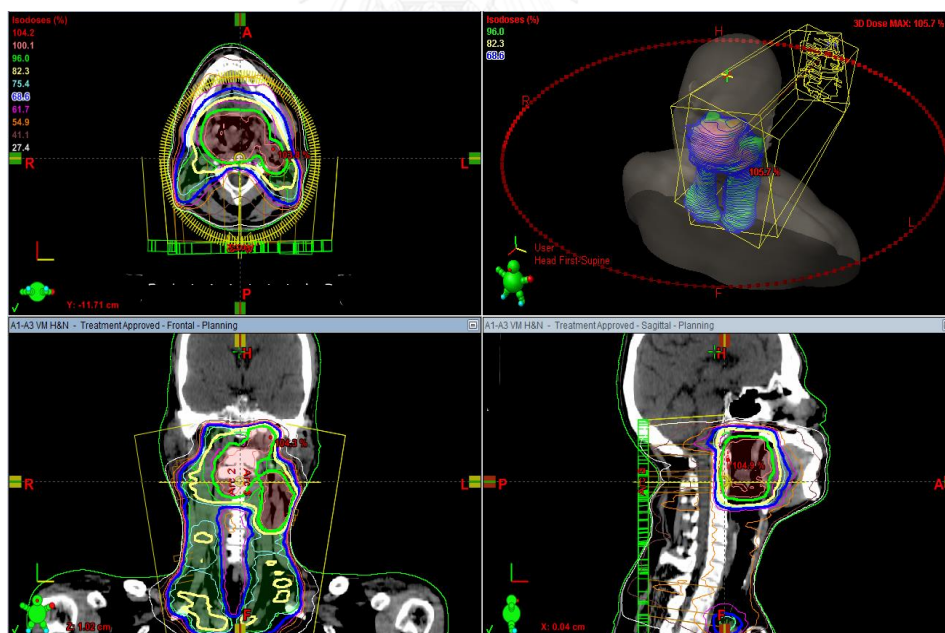
Figure 2.7 Volumetric modulated arc therapy technique

2.1.4 Radiation Detectors

Ionization chambers and solid stale detectors are used in radiotherapy for the determination of radiation dose.

2.1.4.1 Ionization Chambers

Generally, the ionization chambers have the components as shown in figure 2.8. A gas filled cavity is surrounded by a conductive outer wall and equipped with a central collecting electrode. The wall and the collecting electrode are separated with a high quality insulator to reduce the leakage current when a polarizing voltage is applied to the chamber. Another component is a guard electrode. This electrode aims to reduce the probability of chamber leakage. The guard electrode intercepts the leakage current and allows it to flow to ground, by passing the collecting electrode. It also ensures improved field uniformity in the active or sensitive volume of the chamber [17].

The mass of air in the chamber volume is affected by the changes in the ambient temperature and pressure. Therefore, measurement with ionization chambers require temperature and pressure correction (K_{TP}) to address this problem.
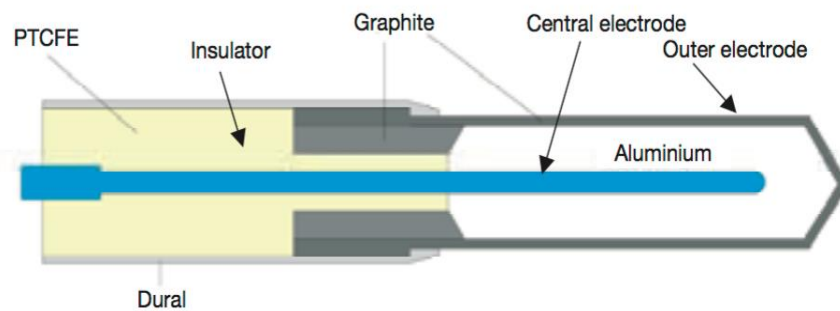
Figure 2. 8 Components of cylindrical Farmer type ionization chamber

In this study, we used CC13 ionization chamber, FC65-P Farmer chamber and diode detector.

A. CC13 Ionization Chamber

The CC13 ionization chamber, as shown in figure 2.9 can be employed to measure the absolute and the relative dosimetry of photon and electron beams in radiotherapy. The chamber has a sensitive volume 0.13 cm^3, total active length 5.8 mm, cylinder length 2.8 mm. The inner diameter of the cylinder is 6.0 mm while the radius of cylinder is 3.4 mm. The thickness of wall material is 0.4 mm, diameter of inner electrode is 1.0 mm, length of electrode 3.3 mm and reference point in water 3.5 mm from the distal end of the chamber. It operates with polarizing voltage ±300 volts [18].

Figure 2. 9 CC13 ionization chamber

B. FC65-P Ionization Chamber

The FC65-P is an ionization chamber of a classic Farmer design, intended for absolute dosimetry of photon and electron beams that meet or exceed performance standard of the original physical dimensions, a choice of thimble material sensitive volume of 0.65 cc and atmospheric communication. Additional features are not shared with the original Famer include guarding up to the measuring volume and waterproof construction. The FC65-P model is most closely resembling the NE 25881A, that it has a rugged thimble made of Delrin (POM, poly-oxymethylate), an aluminum center electrode [19]. The FC65-P ionization chamber is shown in figure 2.10.

Figure 2. 10 FC65-P ionization chamber

2.1.4.2 Diode Detector

Diodes have also been shown to be dose rate dependent, but this problem is much more prominent for the n-type than for the p-type diodes (Rikner and Grusell) [20]. It has also been reported that silicon diodes have an angular dependent response, silicon diodes are convenient for measurements in small photon radiation fields and also used for electron beam measurement. Diodes can be used as radiation detectors since they produce an electrical signal when exposed to ionizing radiation. There are two different ways to use diodes as radiation detectors. One is to the analyze the pulses formed in the diode and create a pulse height spectrum. The other way is to use the diode as dosimeter by measuring the total charge formed in the diode during irradiation. When measuring dose in water phantom the ideal dosimeter should be made of materials similar to water phantom. The use of silicon diodes as dosimeters has many benefits compared to other detectors. The active volume in silicon diodes can be kept small and still produce a high signal (without the need for external bias voltage) since the density is high. The small active volume also give rise to a high spatial resolution, which is beneficial for measuring dose in regions with steep gradients in penumbras and small fields.

For the IBA PFD 3G photon dosimetry diode detector (Schwarzenbruck, Wellhofer), as shown in figure 2.11. The high doped p-type silicon detector chips, specifically designed for radiation therapy applications, have since their introduction in 1992 been the natural choice for measurements where high spatial resolution is required. Its diameter, sensitive volume and sensitive volume thickness are 2.5 mm, 3×10^{-3} cc and 60 µm, respectively. Diode detector is an excellent choice in relative field analysis of profile and output measurement in water phantom because of the small active volume. The accuracy and lifetime of the diode detectors is unsurpassed in the field of radiation therapy. Diode detector provides high sensitivity and good stability in the measurements and exhibits consistent sensitivity with accumulated dose [17].

Figure 2. 11 IBA PFD 3G photon dosimetry diode detector

2.2 Review of Related Literatures

Failla GA., et al., [1] has performed an assessment test in order to assure the dose calculation accuracy in typical and challenging phantom and patient geometries. Acuros XB algorithm provided comparable accuracy in treatment planning conditions to benchmarked Monte Carlo methods for the full range of X-Ray beams produced by clinical linear accelerators 4 MV–25 MV. For example, Monte Carlo methods employed techniques to accelerate solution times or reduce noise. In the explicit LBTE solution methods, errors were primarily systematic and result in a faster solution, but less accuracy.

Hoffmann L., et al., [2] investigated the accuracy of Acuros XB algorithm photon dose calculation algorithm in both homogeneous and heterogeneous phantom geometries. The accuracy of the algorithm was tested in a range of clinical situations including variable SSD, asymmetric fields, for Intensity Modulated Radiation Therapy (IMRT) and Volume Modulated Radiation Therapy (VMAT) treatment plans. The performance of the algorithm was compared to ionization chamber, diamond detector and film measurements relative to calculations within the current standard algorithm (AAA). The measurements were performed using test plan of 6 MV and 15 MV photons on CIRS phantom. Moreover, this study observed the output factors, depth dose curves and beam profiles of symmetric and asymmetric fields. The results showed a good agreement with AAA algorithm. For the plans calculated on the CIRS phantom, the number of field size met the gamma criterion of 3% in dose and 3 mm in DTA was higher with Acuros XB algorithm (98% for 6 MV; 100% for 15 MV) compared to AAA algorithm (94% for 6 MV; 96% for 15 MV). The dose calculations with the Acuros XB algorithm in homogeneous media are in good agreement with both measurements and the AAA algorithm. In heterogeneous media, the Acuros XB algorithm was superior to AAA in both lung and bone materials

Breitman K., et al., [14] reported their works to validate the AAA photon beam dose calculation algorithm factory commissioned using "golden beam data" with the differences between measurements and calculations performed at two institutions using 6 MV and 15 MV beams. The study used two independent analysis methods to compare dose measurements from two different clinical LINACs with AAA calculated doses. The AAA performed well for the conditions tested. Evaluation of measured relative dose profiles revealed that 97%, 99%, 97% and 100% of points at one institute and 96%, 88%, 89% and 100% of points at the other institution passed TG-53 report in the outer beam, penumbra, inner beam and buildup regions, respectively.

Rana S., et al., [15] showed validation of Acuros XB algorithm by performing measurements and Monte Carlo (MC) simulations and reported better dose prediction accuracy using the AXB algorithm than using the AAA in heterogeneous media. Her studied also showed the dosimetric evaluation of both the AXB algorithm and AAA was done based on the RTOG 0813 dosimetric parameters for 14 SBRT cases. The results from that study demonstrated that both the AXB algorithm and AAA could meet the RTOG 0813 dosimetric criteria for the SBRT lung, and the dosimetric values were lower in the AXB algorithm plans rather than in the AAA plans except for the normal lung tissue. For the lung treatment, literature showed the AXB algorithm produced slightly higher relative volume of the normal lung tissue by receiving 20 Gy (V20) than the AAA. But in details, although the AXB algorithm could improve the accuracy of dose calculations and avoid miscalculation of the MUs in the lung cancer treatment plans, it is not yet clear which dose reporting mode in AXB algorithm should be used for a clinical purpose.

CHAPTER III

RESEARCH METHODOLOGY

3.1 Research Design

This study is an observational descriptive design.

3.2 Research Design Model

This research was divided into two major steps as shown in figure 3.1. Step 1 starts from measurement in water phantom to measure beam characteristics of percent depth dose, beam profile and output factor for various filed sizes in the homogeneous medium and compare all the data to treatment planning data. Step 2 of this study is clinical application in three different techniques of 3D-CRT, IMRT and VMAT plans implemented in head, chest and pelvic regions in both homogeneous and inhomogeneous phantoms.
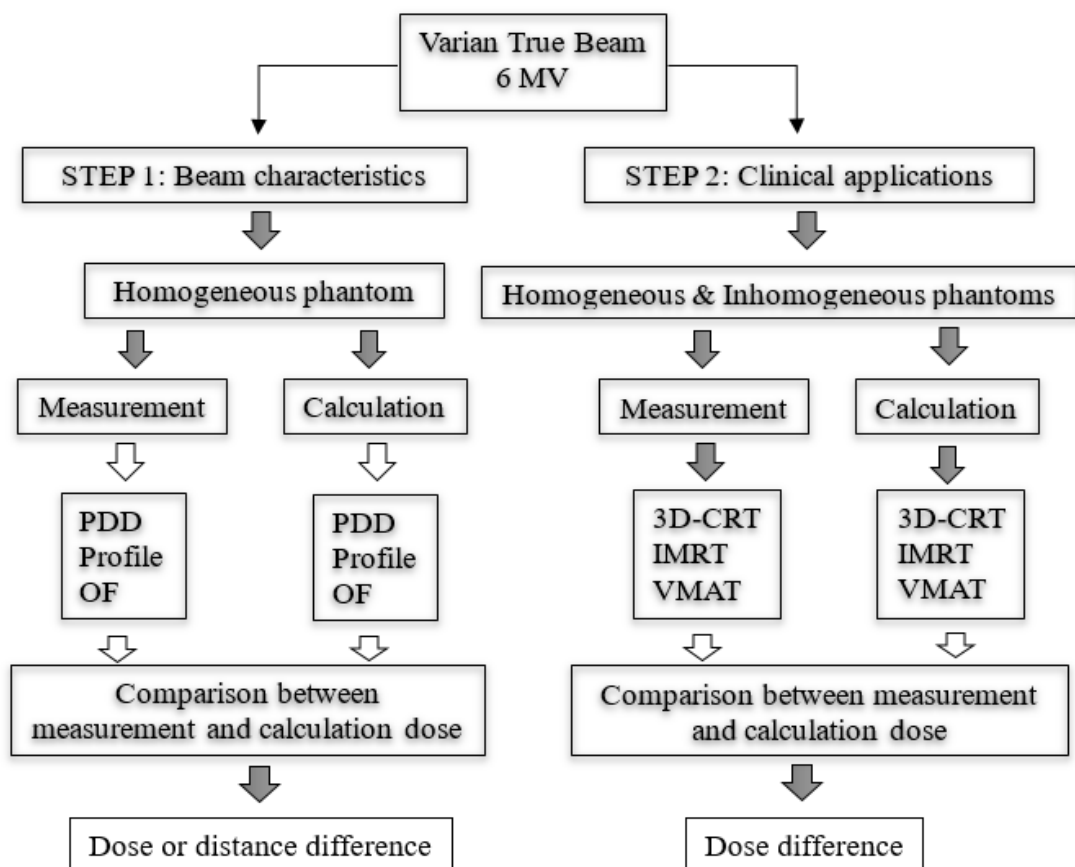
Figure 3.1 Research design model

3.3 Conceptual Framework

In this study, there are some factors affected the percentage dose difference or distance to agreement there are field sizes, field shaped, depth, complexity of plan (3D-CRT, IMRT, VMAT techniques) and phantoms (homogeneous, heterogeneous medium) as shown in figure 3.2.
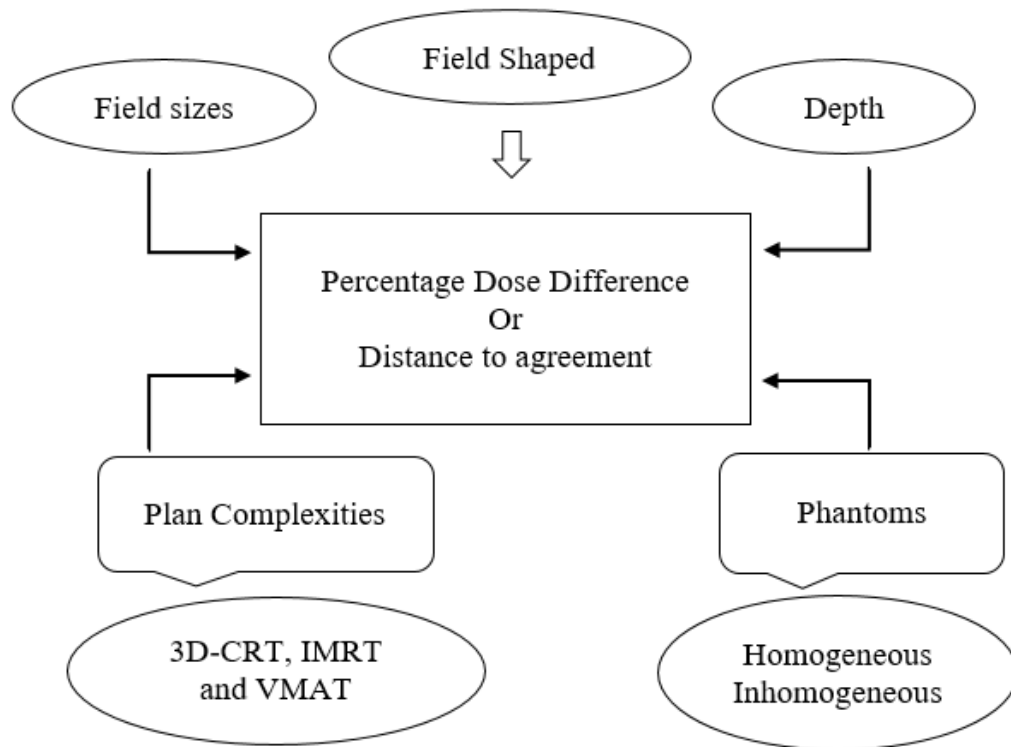
Figure 3.2 Conceptual framework

3.4 Key Words

- Acuros XB algorithm
- Dose verification
- 3D-CRT
- IMRT
- VMAT

3.5 Research Question

What is the dosimetric accuracy in Acuros XB algorithm implemented in the Eclipse™ treatment planning system?

3.6 Materials

3.6.1 Linear Accelerator

The Varian TrueBeam linear accelerator integrates imaging and radiation delivery. It can deliver in 3D-Conformal Radiation Therapy, Intensity Modulated Radiation Therapy (IMRT), RapidArc Radiotherapy, Stereotactic Radiosurgery (SRS) and Stereotactic Body Radiotherapy (SBRT) techniques, all from one system [21].

The Varian TrueBeam Linear accelerator (Varian Medical Systems, Palo Alto, CA, USA), as shown in figure 3.3 provides photon beams of 6 MV and 10 MV (FF and FFF) and various electron beam energies of 6 MeV, 9 MeV, 12 MeV, 15 MeV, 18 MeV and 22 MeV. In this research, only 6 MV photon beams was used.

Figure 3.3 Varian TrueBeam linear accelerator

3.6.2 Eclipse™ Treatment Planning System

The Eclipse™ treatment planning system version 11.0.31 (Varian Medical Systems, Palo Alto, CA, USA), as shown in figure 3.4, is a comprehensive solution that is open, integrated and easy to use. Eclipse™ allows the treatment planning on a variety of modalities from a single platform and streamlines into the planning process with clinical protocols and templates. It can access all records and dosimetry information from one system. Eclipse™ can generate the plans for 3D-CRT, IMRT and VMAT techniques [22].
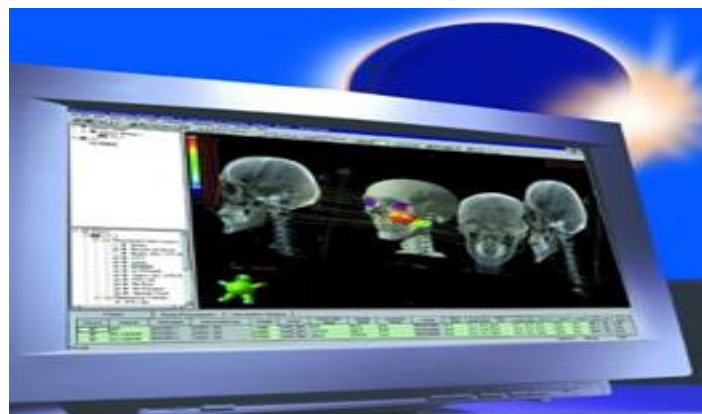
Figure 3.4 Eclipse™ treatment planning software

3.6.3 Blue Water Phantom

The blue phantom, three-dimensional beam analyzing system (IBA Dosimetry GmbH, Schwarzenbruck, Germany), as displays in figure 3.5, is made from acrylic plastic (Perspex), having the scanning volume of 480 x 480 x 410 mm^3. It is prepared for external control from the OmniPro-Accept 6.4a software. This phantom can be used for percent depth dose, beam profile scanning and output factor, measurements with various detector types [23].

Figure 3.5 Blue water phantom

3.6.4 Solid Water Phantom

The solid water phantom (RMI Gammex, Middleton, WI, USA), in this experiment is the material composed of epoxy resins and power control density as the homogeneous phantom and a radiation property within the density of 1.03 g/cm^3. The physical form is made in square slab of 30x30 cm^2 with the thickness variation of 0.2, 0.3, 0.5, 1, 2, 3, 4 and 5 cm as shown in the figure 3.6. The solid water phantom material provides the convenience of a solid water phantom without the need for correction factors and enables to achieve calibration factor within 1% [24].
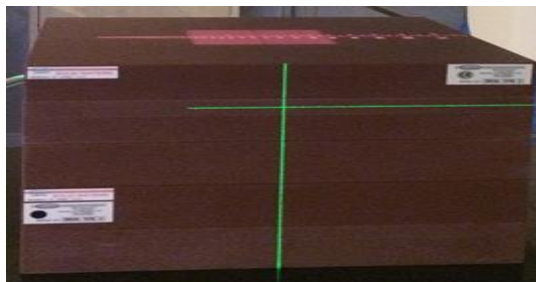
Figure 3.6 Solid water phantoms

3.6.5 CIRS Phantom

The CIRS phantom for film and ion chamber dosimetry is designed to address the complex issues surrounding commissioning and comparison of treatment planning systems while providing a simple yet reliable method for verification of individual patient plans and treatment delivery. Figure 3.7, shows CIRS Model 002LFC IMRT Thorax Phantom (Norfolk, Virginia, USA) [25]. This phantom is elliptical in shape and its property represents an average human torso in proportion, density and 2D structures. CIRS Phantom Model 002LFC phantom consists of different materials, which represent lung, bones and soft tissue organs for heterogeneity purpose. The dimension of this phantom is 30 cm (length) x 30 cm (width) x 20 cm (thick). This phantom has several holes to accommodate ionization chambers for point dose measurements in multiple planes inside the phantom.

Figure 3.7 CIRS phantom (Model 002LFC)

3.6.6 CC13 Ionization Chamber

The CC13 ionization chamber (IBA, Wellhofer Dosimetric, Schwarzenbruck, Germany), as shown in figure 3.8, can measure absolute and relative dosimetry of photon and electron beams in radiotherapy by compact chamber beam scanning in water phantoms [26]. The CC13 has sensitivity of 27×10^7 Gy/C with the active volume of 0.13cc.

Figure 3.8 CC13 ionization chamber

3.6.7 FC65-P Ionization Chamber

The FC65-P (IBA, Wellhofer Dosimetric, Schwarzenbruck, Germany), is an ionization chamber which has sensitive volume of 0.65 cm^3 and total active length 23.1 mm. This ionization chamber is most similar to the NE 2581A, that it has a rugged thimble made of Delrin (POM, poly-oxymethylate) and center electrode which made of an-aluminum [27]. FC65-P is designed preferably for the energy ranges of photons and electrons at medical accelerators shown figure 3.9. This chamber is used for absolute dose measurement, such as output measurement.

Figure 3.9 FC65-P ionization chamber

3.6.8 Diode Detector

The IBA dosimetry PFD diode detectors (IBA, Dosimetry GmbH, Schwarzenbruck, Germany), as shown in figure 3.10, are an excellent choice in relative field analysis for profile measurement in water because of the small active volume. The active volume of this diode detector is 0.19 mm^3. The accuracy and lifetime of the diode detectors is unsurpassed in the field of radiation therapy. Diode detector provides high sensitivity and good stability in the measurements and exhibits consistent sensitivity with accumulated dose. Sensitivity variation of this detector is <0.5%/kGy at 6 MV and <1.5%/kGy at 10 MV [28].

Figure 3.10 Diode detectors

3.6.9 Electrometer

The DOSE-1 (IBA, Wellhofer Dosimetric, DchwarZenbruck, Germany), as displays in figure 3.11 is a portable, single channel, high-precision reference class electrometer for measurements of absorbed dose. The device significantly exceeds the recommendations of the IEC 60731 [29]. Dose, dose rate, average dose rate, charge, current and dose per monitor unit are all measured and displayed simultaneously. Up to 40 detector specific data sets can be stored in a sensor library, including physical and geometrical parameters. The units are Gray, Sievert, Roentgen, Rad, Rem, C/Kg, Ampere and Coulomb at five-digit floating point. Many difference types of ionization chamber may be used and many polarizing voltages can be selected to supply the ionization chamber in used.

Figure 3.11 Dose-1electrometer

3.6.10 Barometer

A barometer as displayed in figure 3.12 (Technology Promotion Association, Thailand-Japan: No. 7069/13P4027), is a piece of equipment that measures air pressure (the force of the air) and shows when the weather changes. The reference condition of standard pressure is 1013 kilopascal (kPa) [30].

Figure 3.12 Barometer

3.6.11 Thermometer

A thermometer shown in figure 3.13 (Technology Promotion Association, Thailand-Japan), is a device that measures temperature or a temperature gradient. The reference condition of standard pressure in absorbed dose determination for external beam radiotherapy based on Technical Report Series 398 is 20 degree Celsius [31].

Figure 3.13 Thermometer

3.7 Methods

The study was divided into two parts: beam characteristics in water phantom and clinical applications with 3D-CRT, IMRT and VMAT techniques of head, chest and pelvic regions in solid water phantom and CIRS phantom.

3.7.1 Beam Characteristics

The beam measurement of beam characteristics of 6 MV photon beam consists of percentage depth doses, beam profiles and output factors.

3.7.1.1 Percentage Depth Doses

In this research, percentage depth doses were scanned from 0 to 30 cm depth at 100 cm SSD setup using CC13 ionization chamber in IBA blue water phantom. Field sizes were designed into open square field sizes of 5x5 cm^2, 10x10 cm^2, 20x20 cm^2, 30x30 cm^2 and open rectangular field sizes of 10x5 cm^2, 20x10 cm^2, 30x10 cm^2.

3.7.1.2 Beam Profiles

In this research, the in-plane and cross-plane profiles were scanned with PFD diode detector in IBA blue water phantom at the depth of 5 cm, 10 cm and 20 cm. Field sizes were set into open square field sizes of 5x5 cm^2, 10x10 cm^2, 20x20 cm^2, 30x30 cm^2 and open rectangular field sizes of 10x5 cm^2, 20x10 cm^2, 30x10 cm^2.

The measured percentage depth dose and the measured beam profiles were compared with calculated percentage depth dose and calculated beam profiles in Acuros XB algorithm Eclipse™ treatment planning system. These results will be assessed by using parameters δ_1, δ_2, δ_3, δ_4 and δ_{50-90} according to AAPM TG-53 and IAEA TRS 430 as explained in chapter 2.

3.7.1.3 Output Factors

The output factor is the ratio obtained from output dose at any field size divided by output dose at reference field size of 10x10 cm^2. In this research, the accuracy of output factor calculations is an important feature in treatment planning system. Output factors were measured at 10 cm depth, 100 cm SSD by using CC13 ionization chamber in IBA blue water phantom. Field sizes were set into open square field sizes of 5x5 cm^2, 8x8 cm^2, 12x12 cm^2, 15x15 cm^2, 20x20 cm^2, 25x25 cm^2, 30x30 cm^2, 35x35 cm^2 and open rectangular field sizes were set into 10x5 cm^2, 5x10 cm^2, 5x15 cm^2, 5x20 cm^2, 5x30 cm^2, 10x15 cm^2, 10x20 cm^2, 10x25 cm^2, 10x30 cm^2, 20x10 cm^2, 30x10 cm^2.

We verified the accuracy of output factor calculations by comparing measured and calculated outputs needed in expected value of 2% difference for delivering 100 monitor units (MUs) at d_{max} in a IBA blue water phantom.

3.7.2 Clinical Applications

This study compared the results obtained from experimental measurements with the results obtained from calculations in three different techniques; Three Dimensional Conformal Radiotherapy (3D-CRT), Intensity Modulated Radiation Therapy (IMRT) and Volumetric Modulated Arc Therapy (VMAT) techniques.

3.7.2.1 Three Dimensional Conformal Radiotherapy Technique

In this research, we selected 15 plans comprised of 3D-CRT plans of 5 head, 5 chest and 5 pelvic regions. The plans were transferred to solid water phantom and CIRS thorax phantom. The doses were measured at 15 cm depth, 85 cm SSD by using CC13 ionization chamber in solid water phantoms. Afterward, we repeated the measurement in CIRS phantom which represented the inhomogeneous medium and the point of measurement was in the inhomogeneous region.

3.7.2.2 Intensity Modulated Radiation Therapy Technique

We selected 15 plans comprised of IMRT plans of 5 head, 5 chest and 5 pelvic regions. The plans were transferred to solid water phantom and CIRS thorax phantom. The doses were measured at 15 cm depth, 85 cm SSD by using CC13 ionization chamber in solid water phantoms. Afterward, we repeated the measurement in CIRS phantom which represented the inhomogeneous medium and the point of measurement was in the inhomogeneous region.

3.7.2.3 Volumetric Modulated Arc Therapy Technique

We selected 15 plans comprised of VMAT plans of 5 head, 5 chest and 5 pelvic regions. The plans were transferred to solid water phantom and CIRS thorax phantom. The doses were measured at 15 cm depth, 85 cm SSD by using CC13 ionization chamber in solid water phantoms. Afterward, we repeated the measurement in CIRS phantom which represented the inhomogeneous medium and the point of measurement was in the inhomogeneous region.

The tolerance of percent dose difference according to AAPM TG-53, IAEA TRS 430 and ICRU Report No 40, are ±3% and ±5% for homogeneous and inhomogeneous phantom, respectively.

In this study, the dose percentage difference was calculated by using the following equation (11):

$$\% \text{ Dose difference} = \frac{\text{DOSE}(calculated) - \text{DOSE}(measured)}{\text{DOSE}(measured)} \times 100\% \qquad (11)$$

3.8 Sample Size Determination

For clinical application cases, the sample sizes were determined by using following equation (12):

$$n = \frac{z_{\alpha/2}^2 * \sigma^2}{d^2} \qquad (12)$$

Where,

Z $\alpha/2$ = 1.96 (95% confidence level)
α = 0.05
Z = 1.96
σ = 0.019 (Variance of difference)
d = 0.01 (Error rate)
n = 13.87

So, the fifteen plans in each technique were selected in this study.

3.9 Outcome Measurement

Outcome measurement was presented as the percentage dose differences and the distance to agreement between measurement and calculation.

3.10 Statistical Analysis

The percentage difference in the dose was investigated between measurement and calculation by Acuros XB algorithm in Eclipse™ treatment planning system.

3.10.1 Evaluation of Percentage Depth Dose

- δ_1 is central axis for high dose, small dose gradient and selected dose difference at 10 cm depth.
- δ_2 is buildup region of central axis of percentage depth dose for high dose, large dose gradient, and selected distance difference at 90% dose.
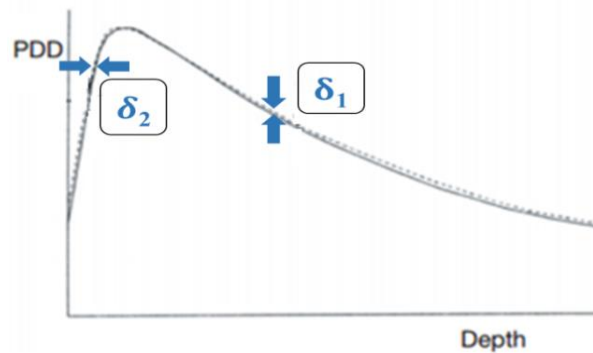
Figure 3.14 Percentage depth dose between measurement and calculation

3.10.2 Evaluation of Beam Profile

- δ_2 is penumbra of profile for high dose, large dose gradient and selected distance difference at 40% dose.
- δ_3 is outside central axis region for high dose, small dose gradient and selected dose difference at 60% of field size.
- δ_4 is outside beam edges for low dose, small dose gradient and selected dose difference at 20% of field size from field edges.
- δ_{50-90} is a beam fringe and selected distance difference at 50% to 90%.
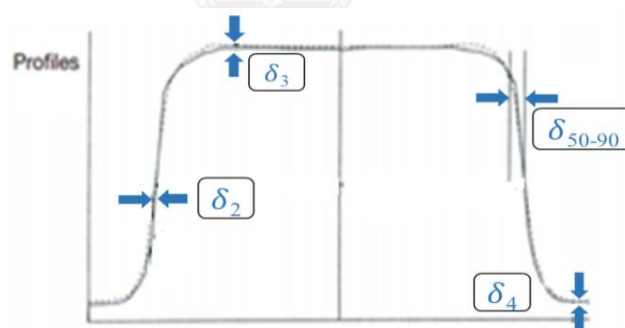
Figure 3.15 Beam profile evaluation between measurement and calculation

3.10.3 Percent Dose Difference

- Range
- Minimum
- Maximum
- Standard deviation

3.10.4 Presentation Format

- Bar graph
- Table

3.10.5 Statistic Software

- Microsoft office excel (2013)

3.11 Ethical Consideration

This study was performed based on the phantoms measurement and calculation by using Acuros XB algorithm in Eclipse treatment planning system version 11.031. The research proposal was submitted and approved by Ethics Committee of Faculty of Medicine, Chulalongkorn University, Bangkok, Thailand.

CHAPTER IV

RESULTS AND DISCUSSION

4.1 Physical Characteristics

4.1.1 Percentage Depth Doses

The scanning percentage depth dose curves along the central axis for 6 MV photon beams at depth of 0-30 cm obtained in the homogeneous water phantom using CC13 ionization chamber were compared with calculations by Acuros XB algorithm.

Figure 4.1, 4.2, 4.3, 4.4, 4.5, 4.6 and 4.7 show the comparison between the measured and calculated percentage depth dose for the square field sizes of 5x5 cm^2, 10x10 cm^2, 20x20 cm^2, 30x30 cm^2 and rectangular field sizes of 10x5 cm^2, 20x10 cm^2, 30x10 cm^2, respectively.
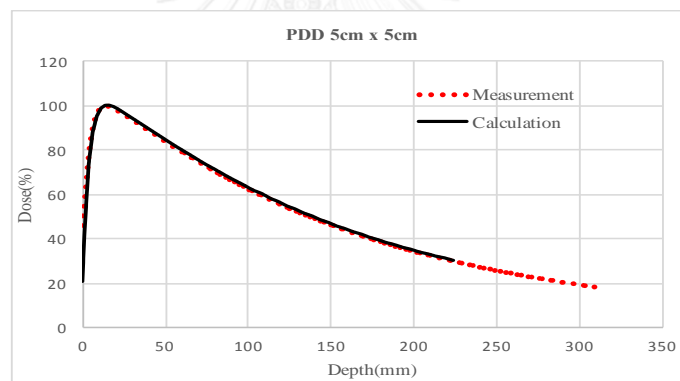
Figure 4.1 Percentage depth dose curve comparisons between measurement and calculation for square field size of 5x5 cm^2
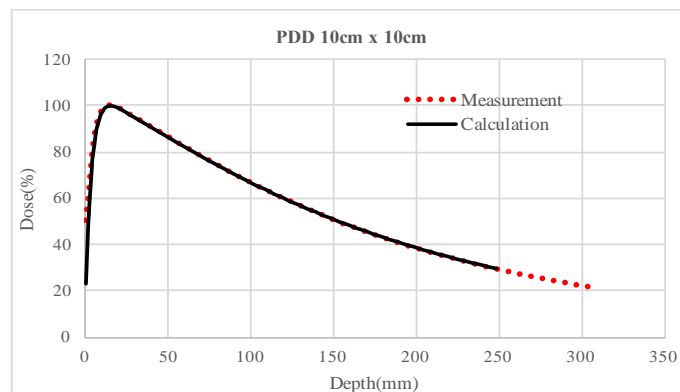
Figure 4.2 Percentage depth dose curve comparisons between measurement and calculation for square field size of 10x10 cm^2
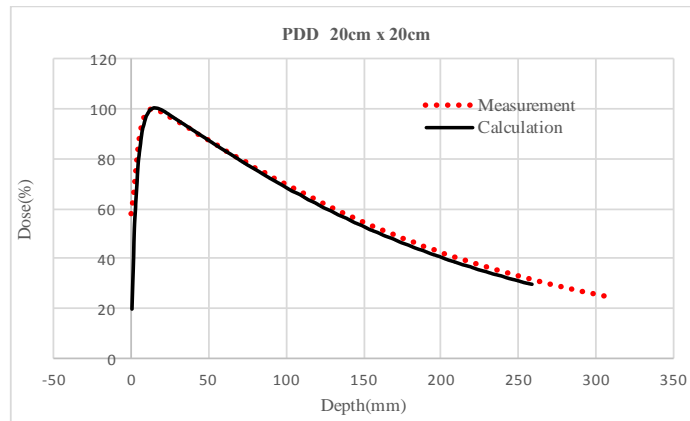
Figure 4.3 Percentage depth dose curve comparisons between measurement and calculation for square field size of 20x20 cm^2
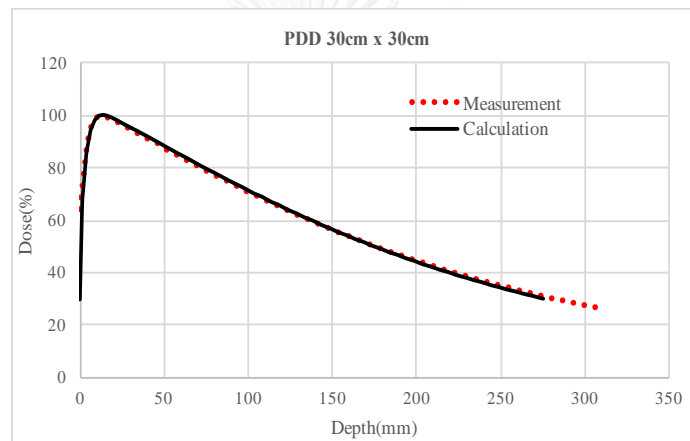
Figure 4.4 Percentage depth dose curve comparisons between measurement and calculation for square field size of 30x30 cm^2
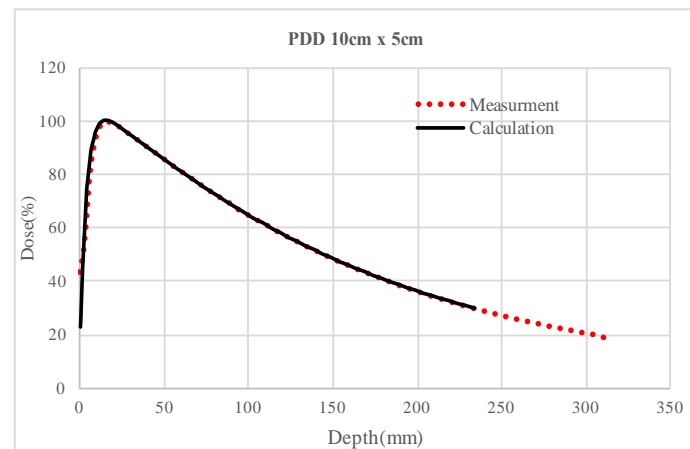
Figure 4.5 Percentage depth dose curve comparisons between measurement and calculation for rectangular field size of 10x5 cm^2
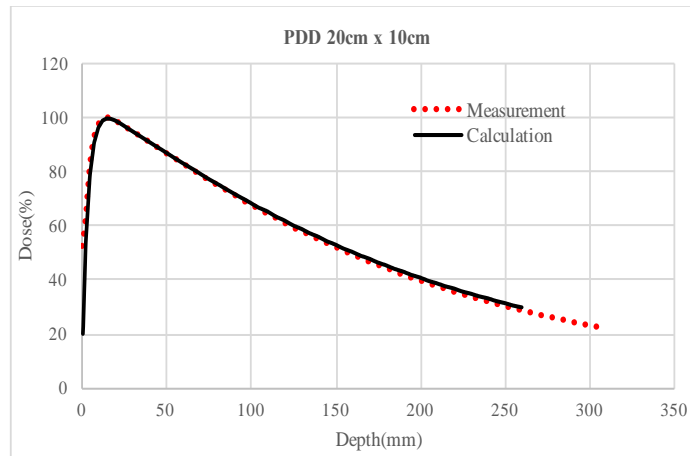
Figure 4.6 Percentage depth dose curve comparisons between measurement and calculation for rectangular field size of 20x10 cm^2
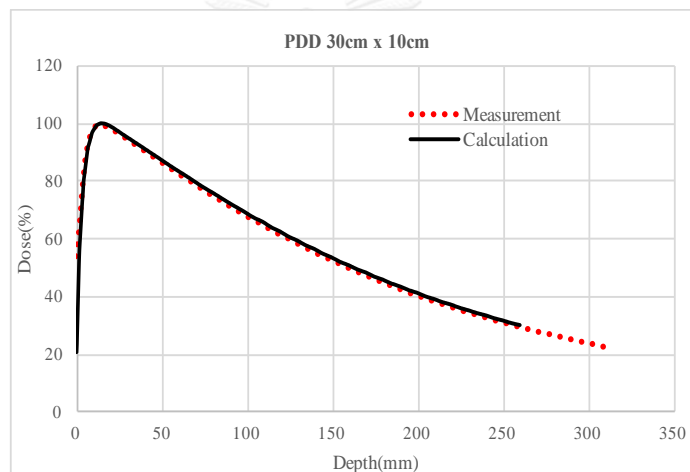
Figure 4.7 Percentage depth dose curve comparisons between measurement and calculation for rectangular field size of 30x10 cm^2

Table 4.1 shows the comparison between the measured and calculated percentage depth dose in term of δ_1 and δ_2 for the square field sizes of 5x5 cm^2, 10x10 cm^2, 20x20 cm^2, 30x30 cm^2 and rectangular field sizes of 10x5 cm^2, 20x10 cm^2, 30x10 cm^2, respectively.

From figure 4.1, 4.2, 4.3, 4.4, 4.5, 4.6 and 4.7, the Acuros XB algorithm calculations are shown in black solid line, while the CC13 ionization chamber measurements are shown as red dotted. The agreement between measured and calculated percentage depth dose for square field size and rectangular size were very good results along the curves (within $\delta_1 = 2\%$ and $\delta_2 = 2$ mm). However, the curves show slightly lower measured doses compared with calculated after buildup region for most all of fields.

Table 4.1 Comparisons of dose (δ_1) and distance (δ_2) differences between measurement and calculation in various square and rectangular field sizes in 6 MV photon beams.

Field size (cm^2)	D 10cm depth		δ_1 (%)	d 90% dose		δ_2 (mm)
	Mea. (%)	Cal. (%)		Mea. (mm)	Cal. (mm)	
5x5	62.40	62.97	0.57	6.38	6.98	0.60
10x10	66.47	66.72	0.25	5.59	6.38	0.79
20x20	69.40	68.24	-1.16	5.25	6.36	1.11
30x30	70.90	71.39	0.49	4.65	5.12	0.47
10x5	64.57	64.45	-0.12	7.76	6.68	-1.08
20x10	67.70	68.24	0.54	5.76	6.36	0.60
30x10	68.00	68.58	0.58	5.71	6.25	0.54
Average			**0.16**			**0.43**
Standard deviation			**0.64**			**0.70**

Following the AAPM TG-53 and IAEA TRS 430, the tolerance limit of δ_1 is 2% and δ_2 is 2 mm. The maximum dose difference at 10 cm depth, δ_1, was found at -1.16% for a 20x20 cm^2 field size, while the maximum distance difference at 90% dose after buildup region, δ_2, was 1.11 mm for a 20x20 cm^2 field size. The smallest dose difference in (δ_1) was found in rectangular field size of 10x5 cm^2, whereas the smallest distance difference (δ_2) was 0.47 mm for square field size 30x30 cm^2.

The average dose difference for all field sizes between measurement and calculation for high dose and small dose gradient of δ_1 was only 0.16±0.64% that agree with **Hoffmann L., et al.,** [2], studied who showed the mean and standard deviation differences of PDD at 10 and 20 cm depth of 0±0.3%. The average distance difference between measurement and calculation for high dose and large dose gradient of δ_2 was 0.43±0.70 mm.

4.1.2 Beam Profiles

In this study, the beam profiles were scanned at 5 cm, 10 cm, and 20 cm depths for in-plane and cross-plane directions with PFD diode detector. The profiles were scanned in blue water phantom for square fields of 5x5 cm^2, 10x10 cm^2, 20x20 cm^2, 30x30 cm^2 and rectangular fields of 10x5 cm^2, 20x 10 cm^2, 30x10 cm^2.

4.1.2.1 Beam Profiles at 5 cm Depth

Figure 4.8, 4.9, 4.10, 4.11, 4.12, 4.13 and 4.14 show the comparison of beam profiles between measurement and calculation at 5 cm depth for the square fields of 5x5 cm^2, 10x10 cm^2, 20x20 cm^2, 30x30 cm^2 and rectangular field size of 10x5 cm^2, 20x10 cm^2, 30x10 cm^2, respectively.

Figure 4.8 In-plane and cross-plane profiles comparison between measurement and calculation for square field size of 5x5 cm^2 at 5 cm depth.
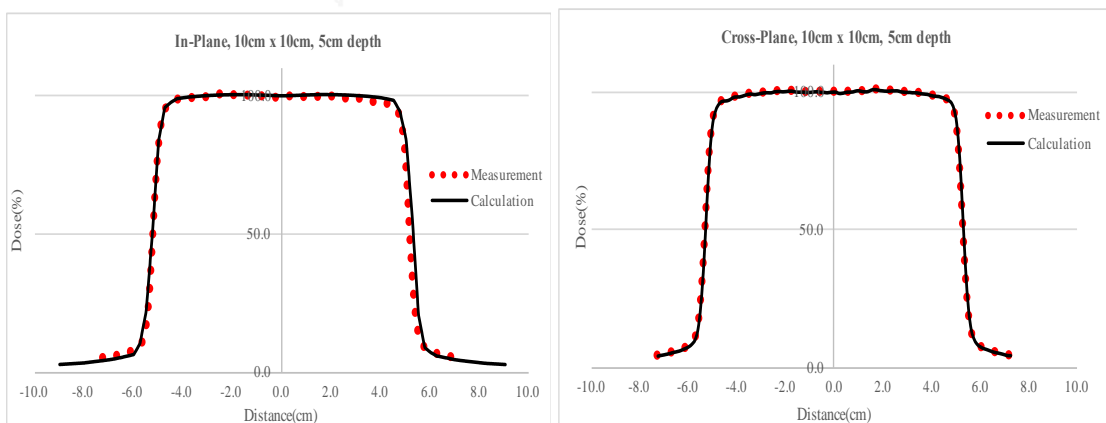
Figure 4.9 In-plane and cross-plane profiles comparison between measurement and calculation for square field size of 10x10 cm^2 at 5 cm depth.
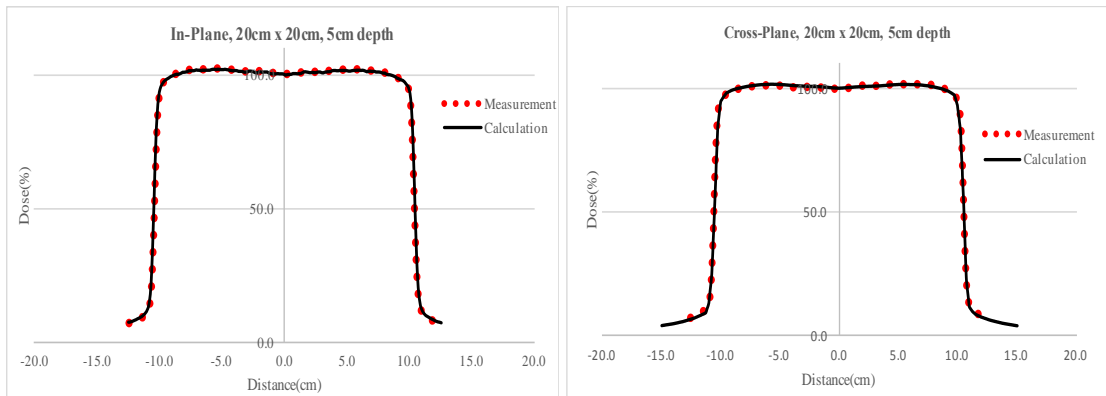
Figure 4.10 In-plane and cross-plane profiles comparison between measurement and calculation for square field size of 20x20 cm^2 at 5 cm depth.

Figure 4.11 In-plane and cross-plane profiles comparison between measurement and calculation for square field size of 30x30 cm^2 at 5 cm depth.

Figure 4.12 In-plane and cross-plane profiles comparison between measurement and calculation for rectangular field size of 10x5 cm^2 at 5 cm depth.

Figure 4.13 In-plane and cross-plane profiles comparison between measurement and calculation for rectangular field size of 20×10 cm^2 at 5 cm depth.

Figure 4.14 In-plane and cross-plane profiles comparison between measurement and calculation for rectangular field size of 30×10 cm^2 at 5 cm depth.

Table 4.2 and 4.3 illustrate the in-plane and cross-plane beam profile comparison between measurement and calculation at 5 cm depth for the square fields of 5×5 cm^2, 10×10 cm^2, 20×20 cm^2, 30×30 cm^2 and rectangular field size of 10×5 cm^2, 20×10 cm^2, 30×10 cm^2, respectively.

For the in-plane and cross-plane profile at 5 cm depth for square and rectangular field sizes, the excellent agreement between measured and calculated percentage differences were observed in all field sizes (within 2 mm for δ_2, 3% for δ_3, 3% for δ_4, and 2 mm for δ_{50-90}). However, the curves showed slightly difference at the penumbra region (δ_{50-90}).

Table 4.2 The in-plane beam profile comparison between measurement and calculation at 5 cm depth in terms of δ_2, δ_3, δ_4 and $\delta_{50\text{-}90}$ for open square and rectangular field sizes.

F.S (cm²)	$d_{40\% \text{ dose}}$ (mm)		δ_2 (mm)	$D_{60\% \text{ inner F.S.}}$ (%)		δ_3 (%)	$D_{20\% \text{outer F.S.}}$ (%)		δ_4 (%)	$d_{50\%\text{-}90\% \text{dose}}$ (mm)		$\delta_{50\text{-}90}$ (mm)
	Mea.	Cal.		Mea.	Cal.		Mea.	Cal.		Mea.	Cal.	
5x5	-26.42	-27.14	-0.72	99.67	99.48	-0.19	6.73	7.03	0.30	3.05	3.53	0.48
10x10	-52.64	-53.38	-0.74	99.98	99.99	0.01	6.54	5.63	-0.91	3.37	4.33	0.96
20x20	-104.99	-106.16	-1.17	101.83	101.48	-0.35	-	-	-	3.33	4.14	0.81
30x30	-157.58	-158.69	-1.11	102.60	102.08	-0.52	-	-	-	3.48	4.59	1.11
10x5	-26.42	-27.04	-0.62	99.53	99.28	-0.25	8.30	8.61	0.31	3.10	3.59	0.49
20x10	-52.67	-53.53	-0.86	99.69	99.80	0.11	7.94	6.96	-0.98	3.30	4.41	1.11
30x10	-52.63	-53.38	-0.75	99.21	99.77	0.56	8.45	7.84	-0.61	3.37	4.43	1.06
Average			-0.85			-0.09			-0.38			0.86
Standard deviation			0.21			0.56			0.64			0.28

The average percent difference between measurement and calculation of in-plane profile at 5 cm depth for penumbra region of profile for high dose, large dose gradient, δ_2 for 40% dose, was -0.85±0.21 mm with the range from -1.17 mm to -0.62 mm. The largest difference of δ_2 was found at 20x20 cm² field, while the smallest error was detected at 10x5 cm² field. For the average percent difference of outside central beam axis for high dose and small dose gradient of δ_3 (60% of field size from central axis) was -0.09±0.56% with the range from -0.52% to 0.56%. The maximum deviation of δ_3 was displayed at 30x10 cm² field size, while the minimum error of δ_3 was seen at 10x10 cm² field size. Our results were better than **Hoffmann L., et al.,** [2], studied who showed the average error at δ_3 about 1%. The average percent difference for outside beam edges for low dose and small dose gradient, δ_4 for 20% of field size from field edge, was -0.38±0.64 with the range from -0.98% to 0.31%. The largest difference of δ_4 was found at 20x10 cm² field, while the smallest error was detected at 5x5 cm² field. The average difference for beam fringe for the distance from 50% to 90% was 0.86±0.28 mm with the range from 0.48 mm to 1.11 mm, while **Hoffmann L., et al.,** [2], presented the DTA deviation at penumbra region above 1mm, especially at large field. The smallest difference of beam fringe was found at 5x5 cm² field, while the largest error was found at 30x30 cm² and 20x10 cm² fields.

Table 4.3 The cross-plane beam profile comparison between measurement and calculation at 5 cm depth in terms of δ_2, δ_3, δ_4 and $\delta_{50\text{-}90}$ for open square and rectangular field sizes.

F.S (cm^2)	$d_{40\%\,dose}$ (mm)		δ_2 (mm)	$D_{60\%\,inner\,F.S}$ (%)		δ_3 (%)	$D_{20\%\,outer\,F.S}$ (%)		δ_4 (%)	$d_{50\%\text{-}90\%dose}$ (mm)		$\delta_{50\text{-}90}$ (mm)
	Mea.	Cal.		Mea.	Cal.		Mea.	Cal.		Mea.	Cal.	
5x5	-26.88	-27.36	-0.48	99.17	99.50	0.33	5.66	6.73	1.07	3.05	3.51	0.46
10x10	-53.56	-53.86	-0.30	99.35	99.91	0.56	6.54	5.33	-1.21	3.14	3.82	0.68
20x20	-106.02	-106.45	-0.43	101.14	101.46	0.32	-	-	-	3.36	4.67	1.31
30x30	-158.38	-157.57	0.81	101.93	102.20	0.27	-	-	-	3.35	4.16	0.81
10x5	-53.20	-53.82	-0.62	99.65	100.26	0.61	4.51	3.78	-0.73	2.95	3.74	0.79
20x10	-105.98	-106.26	-0.28	101.56	101.87	0.31	-	-	-	3.16	4.41	1.25
30x10	-158.36	-158.83	-0.47	102.52	102.83	0.31	-	-	-	3.02	3.75	0.73
Average			**-0.25**			**0.39**			**-0.29**			**0.86**
Standard deviation			**0.48**			**0.14**			**1.20**			**0.31**

For the cross-plane profile, the results showed the same pattern with in-plane profile. The average percent difference between measurement and calculation of cross-plane profile at 5 cm depth for penumbra region of profile for high dose, large dose gradient, δ_2 for 40% dose, was -0.25±0.48 mm with the range from -0.62 mm to 0.81 mm. The highest difference of δ_2 was found at 30x30 cm^2 field, while the lowest error was detected at 20x10 cm^2 field. For the average percent difference of outside central beam axis for high dose and small dose gradient of δ_3 (60% of field size from central axis) was 0.39±0.14% with the range from 0.27% to 0.61%. The maximum deviation of δ_3 was displayed at 10x5 cm^2 field size, while the minimum error of δ_3 was seen at 30x30 cm^2 field size. The average percent difference for outside beam edges for low dose and small dose gradient, δ_4 for 20% of field size from field edge, was -0.29±1.20% with the range from -1.21% to 1.07%. The largest difference of δ_4 was found at 10x10 cm^2 field, while the smallest error was detected at 10x5 cm^2 field. The average difference for beam fringe for the distance from 50% to 90% was 0.86±0.31 mm with the range from 0.46 mm to 1.31 mm. The largest difference of beam fringe was found at 20x20 cm^2 field, while the smallest error was found at 5x5 cm^2 field.

### 4.1.2.2 Beam Profiles at 10 cm Depth

Figure 4.15, 4.16, 4.17, 4.18, 4.19, 4.20 and 4.21 show the comparison of beam profiles between measurement and calculation at 10 cm depth for the square fields of 5x5 cm^2, 10x10 cm^2, 20x20 cm^2, 30x30 cm^2 and rectangular field size of 10x5 cm^2, 20x10 cm^2, 30x10 cm^2, respectively.
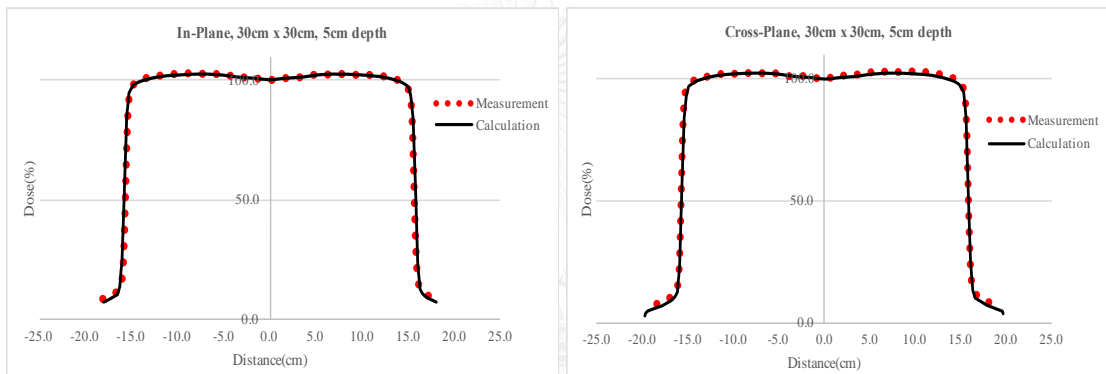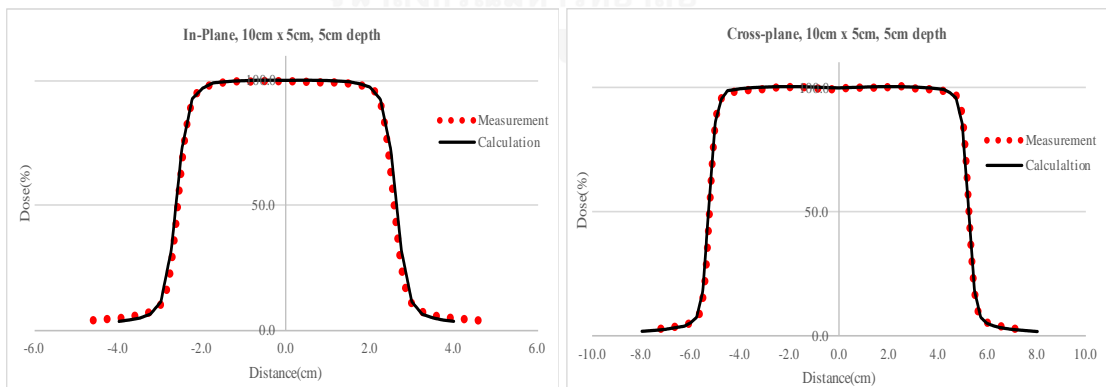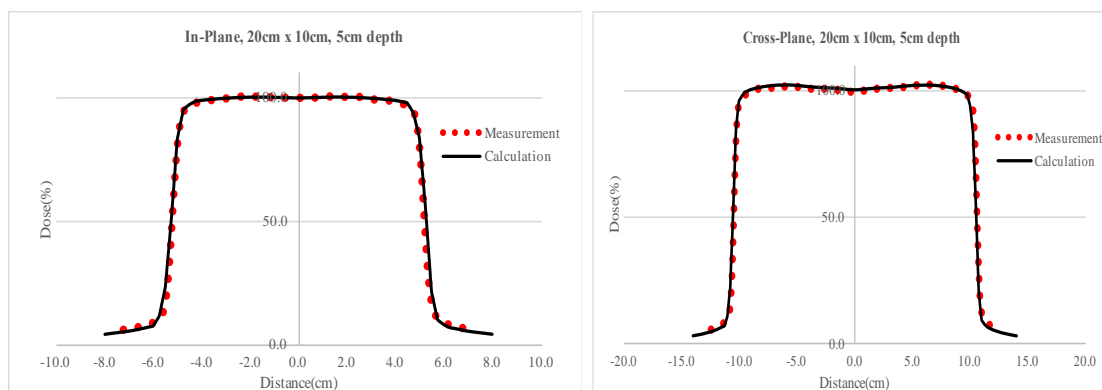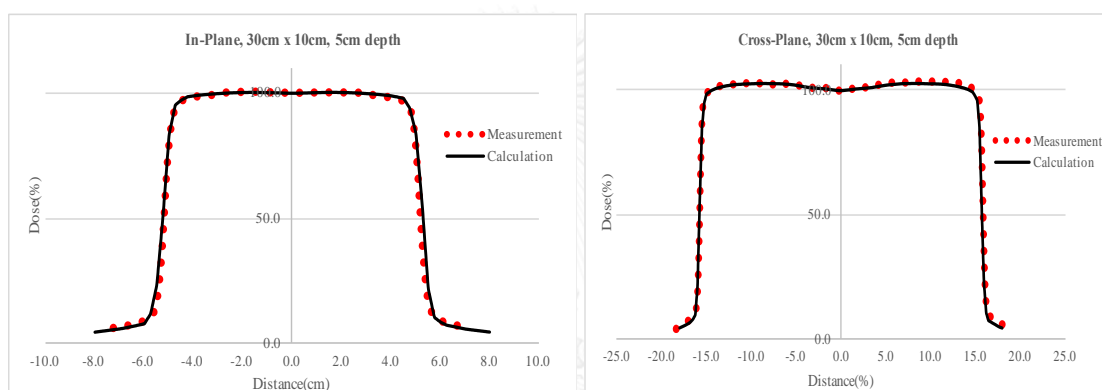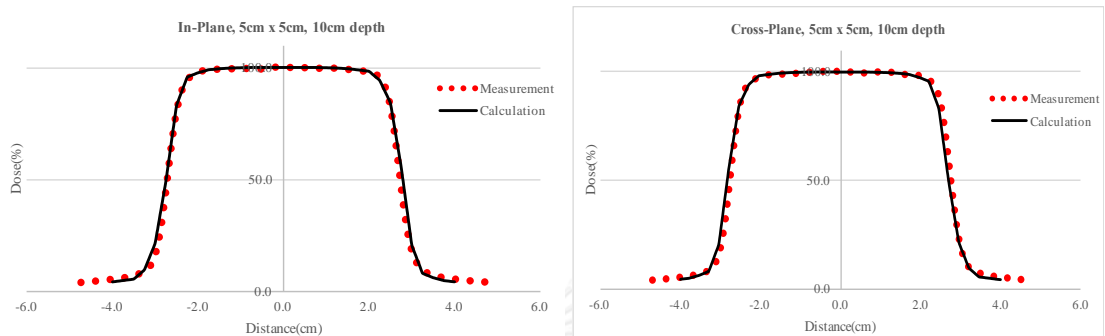

Figure 4.15 In-plane and cross-plane profiles comparison between measurement and calculation for square field size of 5x5 cm^2 at 10 cm depth.
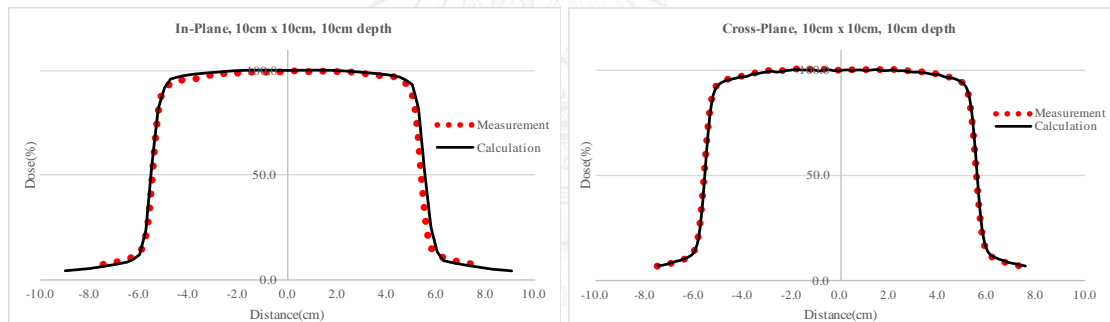
Figure 4.16 In-plane and cross-plane profiles comparison between measurement and calculation for square field size of 10x10 cm^2 at 10 cm depth.

Figure 4.17 In-plane and cross-plane profiles comparison between measurement and calculation for square field size of 20x20 cm^2 at 10 cm depth.

Figure 4.18 In-plane and cross-plane profiles comparison between measurement and calculation for square field size of 30x30 cm^2 at 10 cm depth.

Figure 4.19 In-plane and cross-plane profiles comparison between measurement and calculation for rectangular field size of 10x5 cm^2 at 10 cm depth.

Figure 4.20 In-plane and cross-plane profiles comparison between measurement and calculation for rectangular field size of 20x10 cm^2 at 10 cm depth.

Figure 4.21 In-plane and cross-plane profiles comparison between measurement and calculation for rectangular field size of 30x10 cm^2 at 10 cm depth.

Table 4.4 and 4.5 illustrate the in-plane and cross-plane beam profile comparison between measurement and calculation at 10 cm depth for the square fields of 5x5 cm^2, 10x10 cm^2, 20x20 cm^2, 30x30 cm^2 and rectangular field size of 10x5 cm^2, 20x10 cm^2, 30x10 cm^2, respectively.

For the in-plane and cross-plane profile at 10 cm depth for square and rectangular field sizes, the excellent agreement between measured and calculated percentage differences were observed in all field sizes (within 2 mm for δ_2, 3% for δ_3, 3% for δ_4, and 2 mm for $\delta_{50\text{-}90}$) which were the same as the results at 5 cm depth. However, the curves showed slightly difference at the penumbra region ($\delta_{50\text{-}90}$), (δ_4) but the higher differences were detected compared with 5 cm depth profiles.

Table 4.4 The in-plane beam profile comparison between measurement and calculation at 10 cm depth in terms of δ_2, δ_3, δ_4 and $\delta_{50\text{-}90}$ for open square and rectangular field sizes.

F.S (cm²)	$d_{40\% \text{ dose}}$ (mm)		δ_2 (mm)	$D_{60\% \text{ inner F.S}}$ (%)		δ_3 (%)	$D_{20\% \text{ outer F.S}}$ (%)		δ_4 (%)	$d_{50\%\text{-}90\%\text{dose}}$ (mm)		$\delta_{50\text{-}90}$ (mm)
	Mea.	Cal.		Mea.	Cal.		Mea.	Cal.		Mea.	Cal.	
5x5	-27.80	-28.34	-0.54	99.22	99.14	-0.08	8.84	7.84	-1.00	3.35	4.53	1.00
10x10	-55.63	-56.20	-0.57	97.45	98.78	1.33	9.12	8.32	-0.80	4.17	4.41	0.24
20x20	-110.06	-111.41	-1.35	100.99	100.02	-0.97	-	-	-	5.41	5.11	-0.30
30x30	-165.25	-166.27	-1.02	100.83	100.51	-0.32	-	-	-	6.96	6.63	-0.33
10x5	-27.85	-28.47	-0.62	98.75	99.21	0.46	11.11	10.20	-0.91	3.54	4.47	0.93
20x10	-55.24	-56.22	-0.98	98.44	98.47	0.03	11.31	10.29	-1.02	4.26	4.58	0.32
30x10	-55.23	-56.27	-1.04	98.25	98.42	0.17	12.14	11.01	-1.13	4.22	4.62	0.40
Average			-0.87			0.09			-0.97			0.32
Standard deviation			0.30			0.17			0.12			0.53

The average percent difference between measurement and calculation of in-plane profile at 10 cm depth for penumbra region of profile for high dose, large dose gradient, δ_2 for 40% dose, was -0.87±0.30 mm with the range from -1.35 mm to -0.54 mm. The highest difference of δ_2 was found at 20x20 cm² field, while the lowest error was detected at 5x5 cm² field. For the average percent difference of outside central beam axis for high dose and small dose gradient of δ_3 (60% of field size from central axis) was 0.09±0.17% with the range from -0.97% to 1.33%. The maximum deviation of δ_3 was displayed at 10x10 cm² field size, while the minimum error of δ_3 was seen at 20x10 cm² field size. The average percent difference for outside beam edges for low dose and small dose gradient, δ_4 for 20% of field size from field edge, was -0.97±0.12% with the range from -1.13% to -0.80%. The largest difference of δ_4 was found at 30x10 cm² field, while the smallest error was detected at 10x10 cm² field. The average difference for beam fringe for the distance from 50% to 90% was 0.32±0.53 mm with the range from -0.33 mm to 1.00 mm. The largest difference of beam fringe was found at 5x5 cm² field, while the smallest error was found at 10x10 cm² field.

Table 4.5 The cross-plane beam profile comparison between measurement and calculation at 10 cm depth in terms of δ_2, δ_3, δ_4 and $\delta_{50\text{-}90}$ for open square and rectangular field sizes.

F.S (cm²)	$d_{40\% \text{ dose}}$ (mm)		δ_2 (mm)	$D_{60\% \text{ inner F.S}}$ (%)		δ_3 (%)	$D_{20\% \text{ outer F.S}}$ (%)		δ_4 (%)	$d_{50\%\text{-}90\%\text{dose}}$ (mm)		$\delta_{50\text{-}90}$ (mm)
	Mea.	Cal.		Mea.	Cal.		Mea.	Cal.		Mea.	Cal.	
5x5	-28.26	-29.02	-0.76	98.73	99.17	0.44	8.07	8.25	0.18	3.25	3.78	0.53
10x10	-56.28	-56.37	-0.09	98.93	98.73	-0.20	9.40	7.99	-1.41	3.93	5.01	1.08
20x20	-111.11	-111.59	-0.48	99.43	100.02	0.59	-	-	-	4.88	6.05	1.17
30x30	-166.03	-166.60	-0.57	100.00	100.57	0.57	-	-	-	5.98	6.96	0.98
10x5	-55.88	-56.19	-0.31	98.77	99.42	0.65	6.42	5.46	-0.96	3.54	4.59	1.05
20x10	-111.04	-111.27	-0.23	100.33	100.64	0.31	-	-	-	4.20	5.32	1.12
30x10	-165.94	-166.43	-0.49	100.89	101.44	0.55	-	-	-	4.34	5.52	1.18
Average			**-0.42**			**0.42**			**-0.73**			**1.02**
Standard deviation			**0.22**			**0.29**			**0.82**			**0.23**

The average percent difference between measurement and calculation of cross-plane profile at 10 cm depth for penumbra region of profile for high dose, large dose gradient, δ_2 for 40% dose, was -0.42±0.22 mm with the range from -0.76 mm to -0.09 mm. The highest difference of δ_2 was found at 5x5 cm² field, while the lowest error was detected at 10x10 cm² field. For the average percent difference of outside central beam axis for high dose and small dose gradient of δ_3 (60% of field size from central axis) was 0.42±0.29% with the range from -0.20% to 0.65%. The maximum deviation of δ_3 was displayed at 10x5 cm² field size, while the minimum error of δ_3 was seen at 10x10 cm² field size. The average percent difference for outside beam edges for low dose and small dose gradient, δ_4 for 20% of field size from field edge, was -0.73±0.82% with the range from -1.41% to 0.18%. The largest difference of δ_4 was found at 10x10 cm² field, while the smallest error was detected at 5x5 cm² field. The average difference for beam fringe for the distance from 50% to 90% was 1.02±0.23 mm with the range from 0.53 mm to 1.18 mm. The largest difference of beam fringe was found at 30x10 cm² field, while the smallest error was found at 5x5 cm² field.
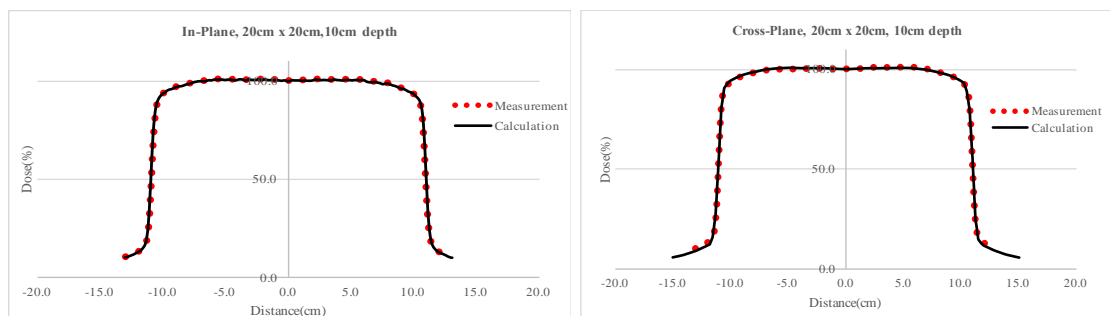
4.2.2.3 Beam Profiles at 20 cm Depth

Figure 4.22, 4.23, 4.24, 4.25, 4.26, 4.27 and 4.28 show the comparison of beam profiles between measurement and calculation at 20 cm depth for the square fields of 5x5 cm^2, 10x10 cm^2, 20x20 cm^2, 30x30 cm^2 and rectangular field size of 10x5 cm^2, 20x10 cm^2, 30x10 cm^2, respectively.
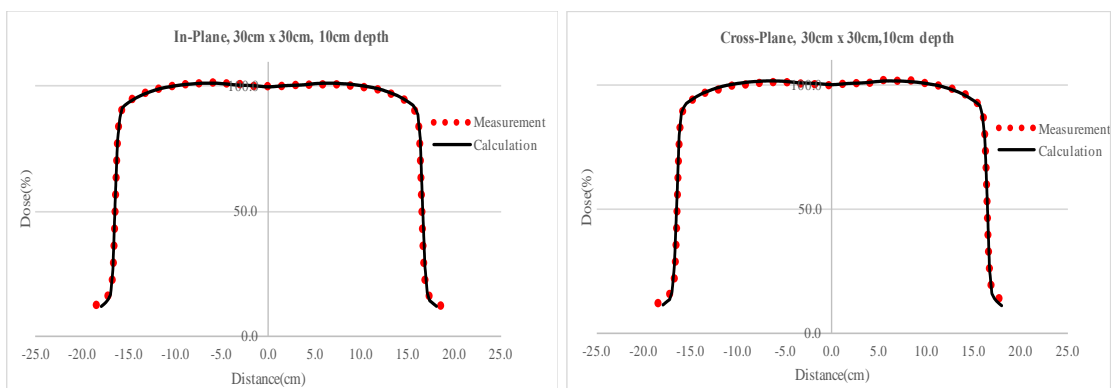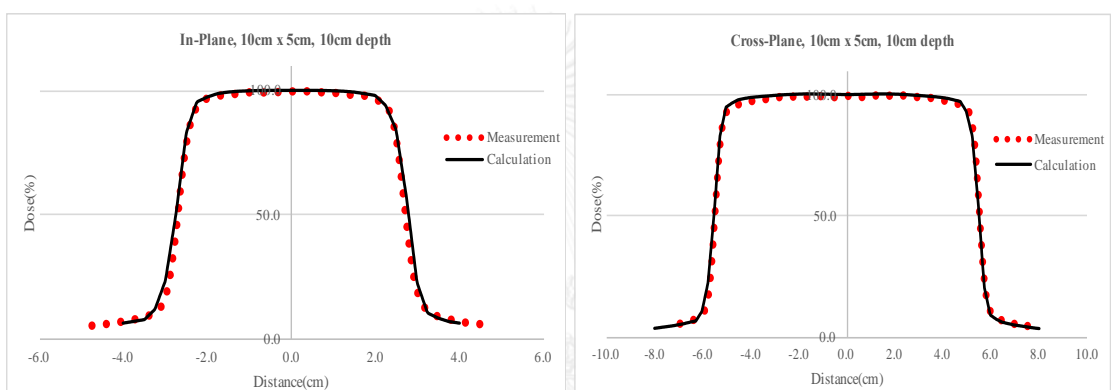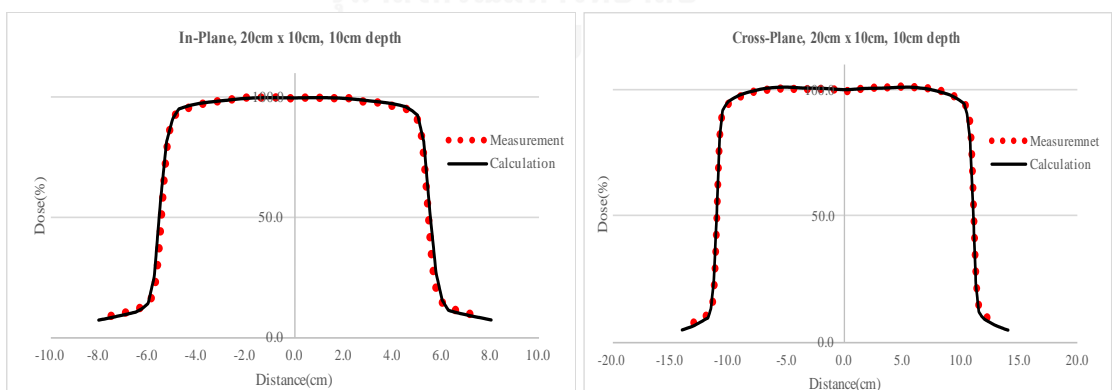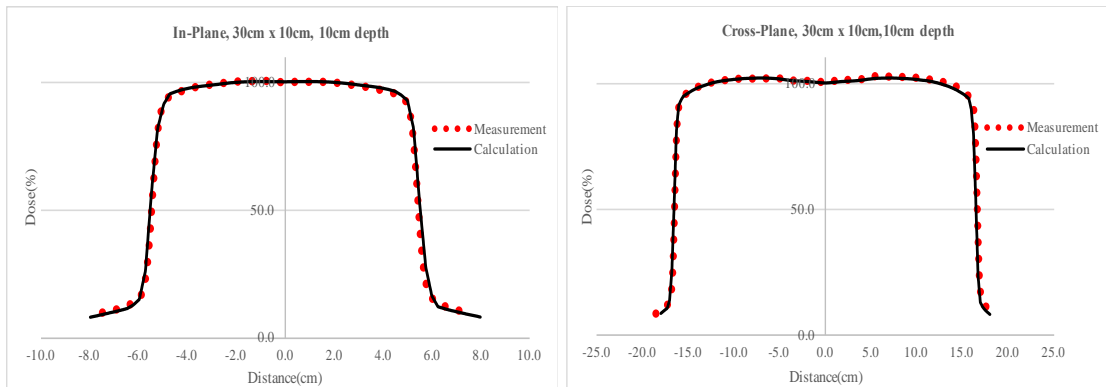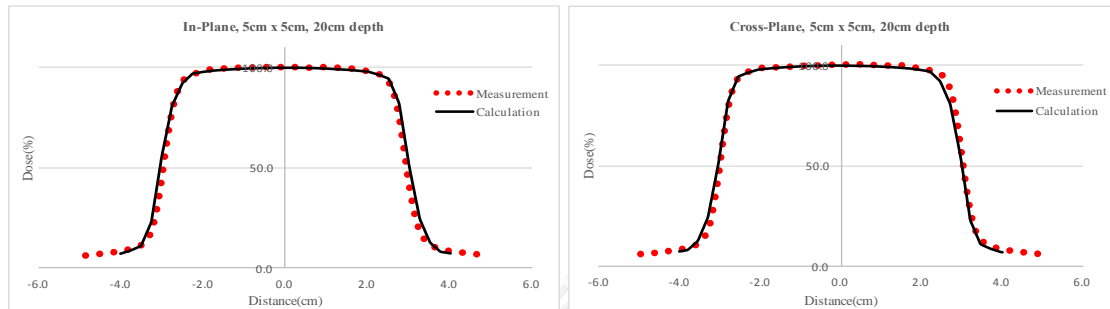

Figure 4. 22 In-plane and cross-plane profiles comparison between measurement and calculation for square field size of 5x5 cm^2 at 20 cm depth.
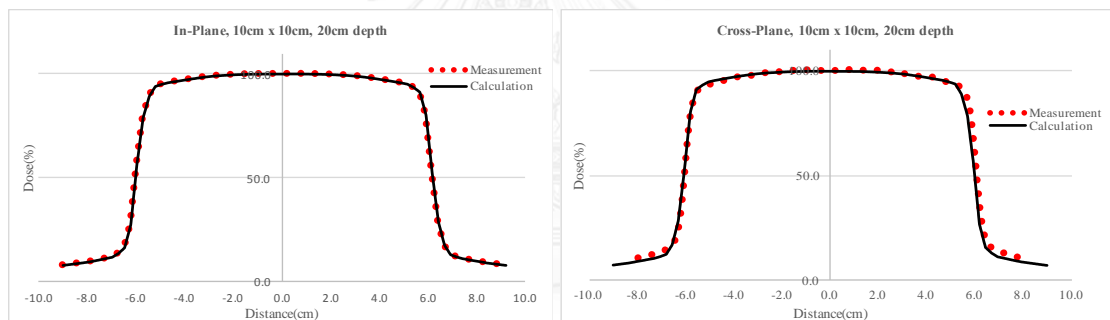
Figure 4.23 In-plane and cross-plane profiles comparison between measurement and calculation for square field size of 10x10 cm^2 at 20 cm depth.

Figure 4.24 In-plane and cross-plane profiles comparison between measurement and calculation for square field size of 20x20 cm^2 at 20 cm depth.
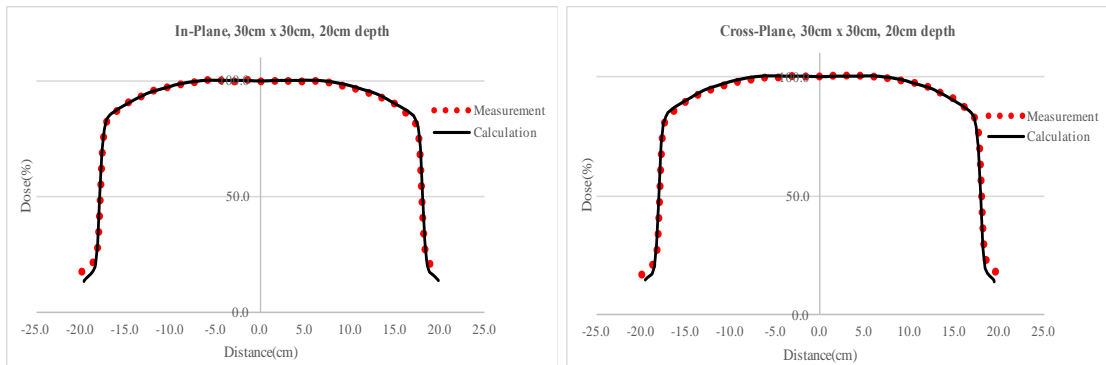
Figure 4.25 In-plane and cross-plane profiles comparison between measurement and calculation for square field size of 30x30 cm^2 at 20 cm depth.
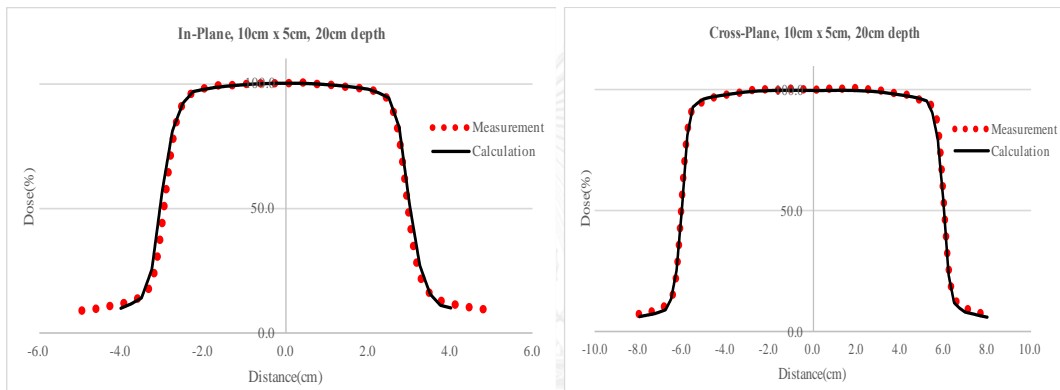
Figure 4.26 In-plane and cross-plane profiles comparison between measurement and calculation for rectangular field size of 10x5 cm^2 at 20 cm depth.

Figure 4.27 In-plane and cross-plane profiles comparison between measurement and calculation for rectangular field size of 20x10 cm^2 at 20 cm depth.
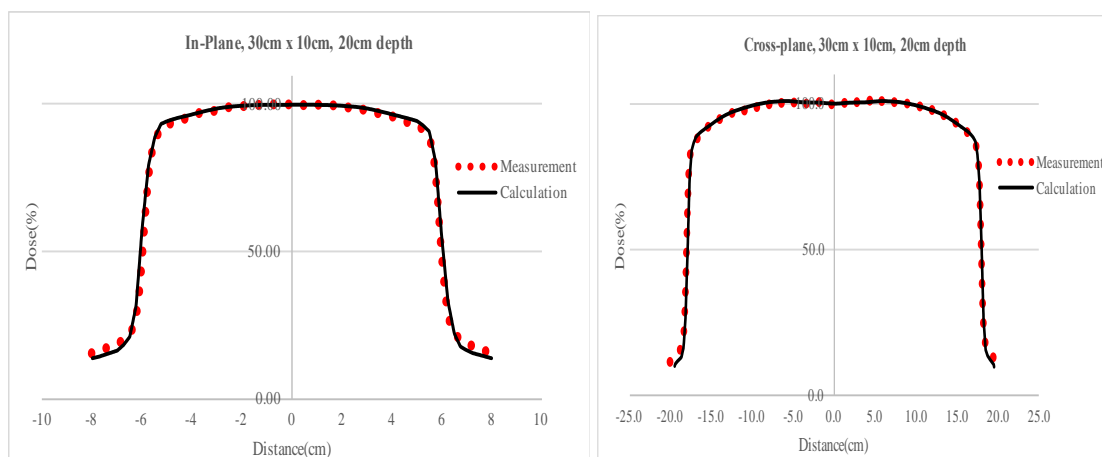
Figure 4.28 In-plane and cross-plane profiles comparison between measurement and calculation for rectangular field size of 30x10 cm^2 at 20 cm depth.

Table 4.6 and 4.7 illustrate the in-plane and cross-plane beam profile comparison between measurement and calculation at 20 cm depth for the square fields of 5x5 cm^2, 10x10 cm^2, 20x20 cm^2, 30x30 cm^2 and rectangular field size of 10x5 cm^2, 20x10 cm^2, 30x10 cm^2, respectively.

The beam profiles at 20 cm depth for in-plane and cross-plane of square and rectangular field sizes showed the excellent agreement between measured and calculated, the percentage differences were found in all field sizes (within 2 mm for δ_2, 3% for δ_3, 3% for δ_4, and 2 mm for δ_{50-90}). However, the curves show slightly difference at the penumbra region (δ_{50-90}) and at lower dose at deeper depth (δ_4).

Table 4.6 The in-plane beam profile comparison between measurement and calculation at 20 cm depth in terms of δ_2, δ_3, δ_4 and $\delta_{50\text{-}90}$ for open square and rectangular field sizes.

| F.S (cm^2)	$d_{40\%\text{ dose}}$ (mm)		δ_2 (mm)	$D_{60\%\text{ inner F.S}}$ (%)		δ_3 (%)	$D_{20\%\text{ outer F.S}}$ (mm)		δ_4 (%)	$d_{50\%\text{-}90\%\text{dose}}$ (%)		$\delta_{50\text{-}90}$ (mm)
	Mea.	Cal.		Mea.	Cal.		Mea.	Cal.		Mea.	Cal.	
5x5	-30.31	-31.15	-0.84	98.84	98.39	-0.45	11.00	10.76	-0.24	3.77	4.09	0.32
10x10	-60.28	-61.13	-0.85	97.93	97.86	-0.07	12.81	11.75	-1.06	5.46	5.02	-0.44
20x20	-120.39	-121.56	-1.17	96.98	97.73	0.75	-	-	-	12.75	11.77	-0.98
30x30	-180.42	-181.25	-0.83	97.03	96.92	-0.11	-	-	-	30.12	29.89	-0.23
10x5	-30.51	-31.37	-0.86	99.03	98.08	-0.95	14.36	14.02	-0.34	3.96	4.26	0.33
20x10	-60.56	-61.70	-1.14	97.46	97.68	0.22	16.33	14.69	-1.64	5.51	5.26	-0.25
30x10	-60.59	-61.72	-1.13	97.31	97.59	0.28	17.64	15.84	-1.80	5.88	5.35	-0.53
Average			-0.97			-0.05			-1.02			-0.25
Standard deviation			0.16			0.55			0.72			0.47

The average percent difference between measurement and calculation of in-plane profile at 20 cm depth for penumbra region of profile for high dose, large dose gradient, δ_2 for 40% dose, was -0.97±0.16 mm with the range from -1.17 mm to -0.83 mm. The highest difference of δ_2 was found at 20x20 cm^2 field, while the lowest error was detected at 30x30 cm^2 field. For the average percent difference of outside central beam axis for high dose and small dose gradient of δ_3 (60% of field size from central axis) was -0.05±0.55% with the range from -0.95% to 0.75%. The maximum deviation of δ_3 was displayed at 10x5 cm^2 field size, while the minimum error of δ_3 was seen at 10x10 cm^2 field size. The average percent difference for outside beam edges for low dose and small dose gradient, δ_4 for 20% of field size from field edge, was -1.02±0.72% with the range from -1.80% to -0.24%. The largest difference of δ_4 was found at 30x10 cm^2 field, while the smallest error was detected at 5x5 cm^2 field. The average difference for beam fringe for the distance from 50% to 90% was -0.25±0.47 mm with the range from -0.98 mm to 0.33 mm. The largest difference of beam fringe was found at 20x20 cm^2 field, while the smallest error was found at 30x30 cm^2 field.

Table 4.7 The cross-plane beam profile comparison between measurement and calculation at 20 cm depth in terms of δ_2, δ_3, δ_4 and $\delta_{50\text{-}90}$ for open square and rectangular field sizes.

F.S (cm²)	$d_{40\% \text{ dose}}$ (mm)		δ_2 (mm)	$D_{60\% \text{ inner F.S}}$ (%)		δ_3 (%)	$D_{20\% \text{ outer F.S}}$ (%)		δ_4 (%)	$d_{50\%\text{-}90\%\text{dose}}$ (mm)		$\delta_{50\text{-}90}$ (mm)
	Mea.	Cal.		Mea.	Cal.		Mea.	Cal.		Mea.	Cal.	
5x5	-30.88	-31.38	-0.50	98.26	98.48	0.22	10.43	9.56	-0.87	3.78	4.92	1.14
10x10	-61.48	-61.77	-0.29	97.51	97.95	0.44	12.94	10.97	-1.97	5.28	5.98	0.70
20x20	-121.40	-121.83	-0.43	97.44	97.39	-0.05	-	-	-	14.36	12.44	-1.92
30x30	-181.16	-181.23	-0.07	96.43	97.06	0.63	-	-	-	29.42	30.03	0.61
10x5	-60.05	-61.45	-1.40	98.59	98.79	0.20	8.98	7.41	-1.57	4.16	5.22	1.06
20x10	-121.25	-121.63	-0.38	97.76	98.56	0.80	-	-	-	9.07	7.60	-1.47
30x10	-180.88	-180.75	0.13	97.85	98.73	0.88	-	-	-	17.07	15.30	-1.77
Average			-0.42			0.45			-1.47			-0.24
Standard deviation			0.48			0.34			0.56			1.41

The average percent difference between measurement and calculation of cross-plane profile at 20 cm depth for penumbra region of profile for high dose, large dose gradient, δ_2 for 40% dose, was -0.42 ± 0.48 mm with the range from -1.40 mm to 0.13 mm. The highest difference of δ_2 was found at 10x5 cm² field, while the lowest error was detected at 30x30 cm² field. For the average percent difference of outside central beam axis for high dose and small dose gradient of δ_3 (60% of field size from central axis) was $0.45\pm0.34\%$ with the range from -0.05% to 0.88%. The maximum deviation of δ_3 was displayed at 30x10 cm² field size, while the minimum error of δ_3 was seen at 20x20 cm² field size. The average percent difference for outside beam edges for low dose and small dose gradient, δ_4 for 20% of field size from field edge, was $-1.47\pm0.56\%$ with the range from -1.97% to -0.87%. The largest difference of δ_4 was found at 5x5 cm² field, while the smallest error was detected at 10x10 cm² field. The average difference for beam fringe for the distance from 50% to 90% was -0.24 ± 1.41 mm with the range from -1.92 mm to 1.14 mm. The largest difference of beam fringe was found at 20x20 cm² field, while the smallest error was found at 30x30 cm² field. Our deviation at penumbra was very excellent when compared with **Hoffmann L., et al.,** [2], studied who showed the deviation up to 20% of dose and 6 mm of distance at penumbra region with the large field size and large depth. However, our deepest depth in our study was only 20 cm depth.

4.1.3 Output Factors

The measurement and calculation of output factors for 6 MV photon beams are shown in table 4.8. In these measurements, the field sizes were varied by the square field sizes from 5x5 cm^2 to 35x35 cm^2, and rectangular field sizes from 10x5 cm^2 to 30x10 cm^2 with the reference from 10x10 cm^2.

Table 4.8 The measured and calculated output factors for square and rectangular fields.

Field size (cm^2)	Measurement	Calculation	Difference (%)
5x5	0.90	0.89	-0.46
8x8	0.97	0.96	-0.37
12x12	1.03	1.03	-0.13
15x15	1.06	1.06	0.02
20x20	1.10	1.10	0.00
25x25	1.13	1.13	0.02
30x30	1.16	1.14	-1.49
35x35	1.17	1.15	-1.54
10x5	0.94	0.93	-1.22
5x10	0.93	0.94	0.59
5x15	0.95	0.96	1.05
5x20	0.95	0.96	1.12
5x30	0.96	0.97	1.14
10x15	1.02	1.03	0.42
10x20	1.04	1.04	0.57
10x25	1.04	1.05	0.71
10x30	1.05	1.06	0.80
20x10	1.04	1.04	-0.44
30x10	1.06	1.05	-0.85
Average			**0.61**
Standard deviation			**0.85**

The average output factors difference between measurement and calculation was 0.61±0.85% with the range from -1.54 to 1.14%. The minimum difference that found in the square field size of 20x20 cm^2 and the maximum difference were shown in the square field size of 35x35 cm^2. From the results, it seems to be the lesser deviation was detected at the small field. Our results showed slightly the larger differences than **Hoffmann L., et al.,** [2], who showed the maximum deviation of output factor at 0.5% that might be due to the small chamber selected in our measurement. However, our output factor results were still within the limitation of 2% for all field sizes [11].

4.2 Clinical Applications

In this part, the measurement was performed in solid water phantom as the homogeneous medium and in CIRS phantom as the inhomogeneous medium. The fifteen cases in each 3D, IMRT and VMAT techniques were randomly selected in head, chest and pelvic regions.

4.2.1 Homogeneous Medium in Solid Water Phantom

Figure 4.29 and table 4.9, 4.10 4.11 show percentage of dose differences for 3D-CRT, IMRT and VMAT plans in head (No. 1 to 5), chest (No. 6 to 10) and pelvic (No. 11 to 15). In 3D-CRT, the differences were almost comparable and small deviation in all cases for all regions as shown in circle blue in figure 4.29. It was due to the simple plan in 3D-CRT. On the other hand, IMRT and VMAT as the complicated plans, the difference was slightly high compared with 3C-CRT, however, the results were still within control limits of ± 3%. In IMRT plans, the measured doses were higher than calculated dose for all cases. In contrast with IMRT, the VMAT plans showed lower measured doses than calculated doses. The variation among head, chest and pelvic regions are not much difference because these plans were recalculated in homogeneous water phantom. Therefore, the inhomogeneity correction was not considered.
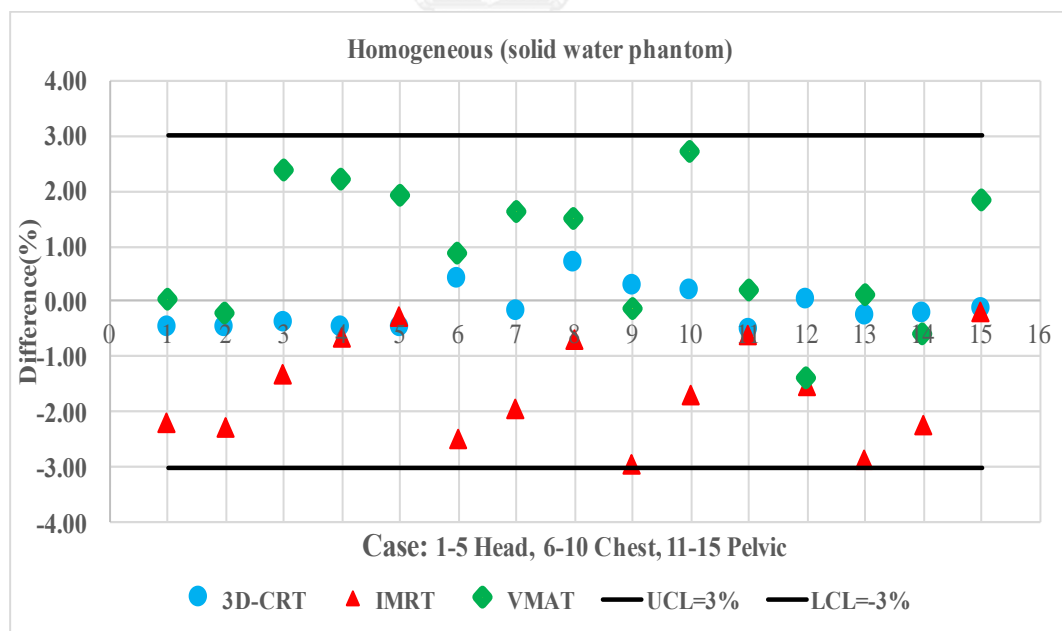
Figure 4.29 The percentage of dose difference between measurement and calculation in 3D-CRT, IMRT and VMAT plans of head, chest and pelvic region in homogeneous solid water phantom.

Table 4.9 shows the results of the clinical cases in 3D-CRT plans in head, chest and pelvic regions by calculating from Acuros XB algorithm and measuring from ionization chamber in homogeneous solid water phantom. The results were very good agreement between measurement and calculation with average dose differences of only -0.12±0.38% with the error range from -0.52 to 0.71%. However, the errors from all the test cases were still within ±3.00% limitation defined by AAPM TG-53.

Table 4.9 The dose difference between measurement and calculation in solid water phantom as the homogeneous medium for 3D-CRT technique.

Case No.	Regions	Measurement (cGy)	Calculation (cGy)	Difference (%)
1	Head	301.35	300	-0.45
2	Head	301.35	300	-0.45
3	Head	301.16	300	-0.38
4	Head	301.40	300	-0.47
5	Head	301.35	300	-0.45
6	Chest	298.76	300	0.42
7	Chest	300.52	300	-0.17
8	Chest	198.58	200	0.71
9	Chest	299.1	300	0.30
10	Chest	199.61	200	0.19
11	Pelvic	180.94	180	-0.52
12	Pelvic	179.96	180	0.02
13	Pelvic	180.45	180	-0.25
14	Pelvic	180.35	180	-0.19
15	Pelvic	180.25	180	-0.14
		Average		**-0.12**
		Standard deviation		**0.38**

Table 4.10 is the results performed the clinical cases in IMRT plans in head, chest and pelvic regions by calculating from Acuros XB algorithm and measuring from ionization chamber in homogeneous solid water phantom. The measured doses were higher than calculated doses for all cases. The average dose differences were -1.59±0.93% with the error range from -2.95 to -0.18% that were higher than in 3D-CRT and VMAT techniques. It was because IMRT plan was more complicated plan and the chamber position may be located in the high dose gradient region. However, the errors from all the test cases were still within ±3.00% limitation defined by AAPM TG-53.

Table 4.10 The dose difference between measurement and calculation in solid water phantom as the homogeneous medium for IMRT technique.

Case No.	Regions	Measurement (cGy)	Calculation (cGy)	Difference (%)
1	Head	306.75	300	-2.20
2	Head	204.69	200	-2.29
3	Head	202.63	200	-1.30
4	Head	201.28	200	-0.63
5	Head	200.53	200	-0.26
6	Chest	205.12	200	-2.49
7	Chest	203.95	200	-1.94
8	Chest	201.36	200	-0.67
9	Chest	206.07	200	-2.95
10	Chest	203.45	200	-1.70
11	Pelvic	181.09	180	-0.60
12	Pelvic	203.08	200	-1.52
13	Pelvic	236.77	230	-2.85
14	Pelvic	229.10	224	-2.22
15	Pelvic	200.37	200	-0.18
Average				-1.59
Standard deviation				0.93

Table 4.11 displays the results of VMAT plans in head, chest and pelvic regions by calculating from Acuros XB algorithm and measuring from ionization chamber in homogeneous solid water phantom. The average dose differences were 0.87±1.24% with the error range from -1.38 to 2.70% that were higher than in 3D-CRT technique due to the complicated plan than 3D-CRT. However, the errors from all the test cases were still within ±3.00% limitation defined by AAPM TG-53. The results were agreed with **Han T., et al.,** [5], experiments that presented the dose differences in range of 0.1% to 3.6%.

Table 4.11 The dose difference between measurement and calculation in solid water phantom as the homogeneous medium for VMAT technique.

Case No.	Regions	Measurement (cGy)	Calculation (cGy)	Difference (%)
1	Head	179.91	180	0.05
2	Head	200.44	200	-0.22
3	Head	202.63	200	2.37
4	Head	201.28	200	2.23
5	Head	200.53	200	1.92
6	Chest	205.12	200	0.89
7	Chest	203.95	200	1.63
8	Chest	201.36	200	1.52
9	Chest	206.07	200	-0.14
10	Chest	203.45	200	2.70
11	Pelvic	179.65	180	0.19
12	Pelvic	182.51	180	-1.38
13	Pelvic	199.74	200	0.13
14	Pelvic	181.09	180	-0.60
15	Pelvic	294.63	300	1.82
Average				**0.87**
Standard deviation				**1.24**

4.2.2 Inhomogeneous Medium in CIRS Phantom

The CIRS phantom was used as the inhomogeneous medium to compare the dose differences between measurement and calculation. The results show very good agreement in all regions and all treatment techniques, especially in 3D-CRT, as shown in figure 4.30 and table 4.12, 4.13, 4.14 because Acuros XB algorithm was designed to improve the accuracy dose calculation in heterogeneity medium than the previous calculation algorithm, AAA.

Figure 4.30 shows the dose differences for 3D-CRT, IMRT and VMAT plans in CIRS phantom for head (No. 1 to 5), chest (No. 6 to 10) and pelvic (No. 11 to 15) regions. In 3D-CRT, the differences were almost the same pattern with the results from homogeneous phantom. The 3D-CRT (blue circle) exhibited the less dose differences compared with IMRT (red triangle) and VMAT (green diamond) techniques.

Figure 4.30 The percentage of dose difference between measurement and calculation in 3D-CRT, IMRT and VMAT plans of head, chest and pelvic region in CIRS inhomogeneous phantom.

Table 4.12 shows the results of the clinical cases in 3D-CRT plans in head, chest and pelvic regions by calculating from Acuros XB algorithm and measuring from ionization chamber in CIRS inhomogeneous phantom. The results were very good agreement between measurement and calculation with average dose differences of only 0.27±0.29% with the error range from -0.37 to 0.61%. However, the errors from all the test cases were still within ±5.00% limitation defined by ICRU Report No 40.
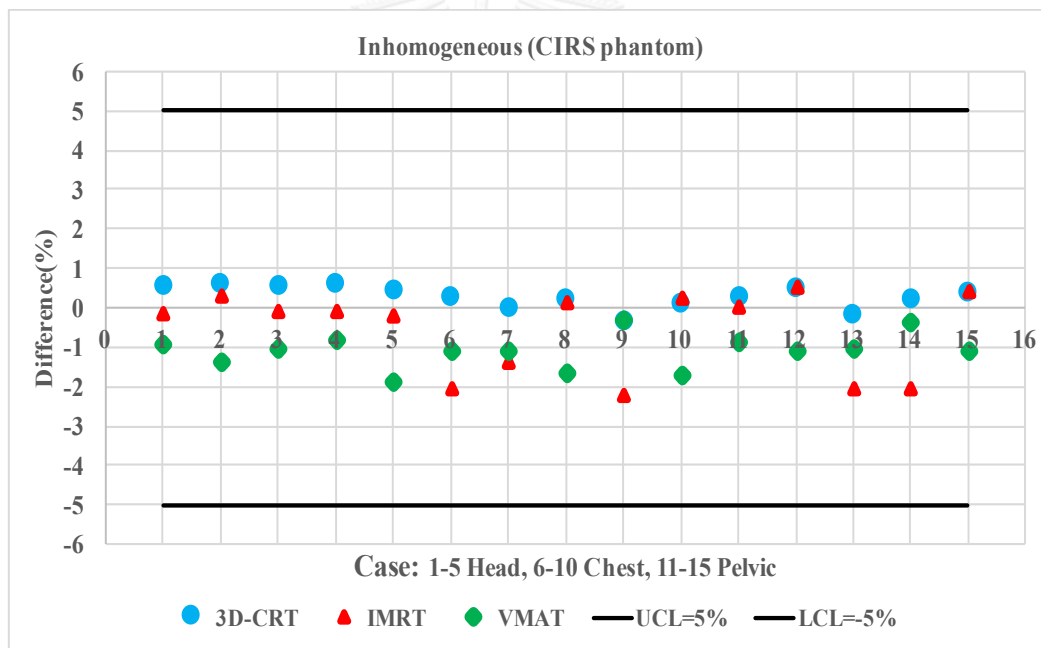
Table 4.12 The dose difference between measurement and calculation in CIRS phantom as the inhomogeneous medium for 3D-CRT technique.

Case No.	Regions	Measurement (cGy)	Calculation (cGy)	Difference (%)
1	Head	298.44	300	0.52
2	Head	298.17	300	0.61
3	Head	298.44	300	0.52
4	Head	298.17	300	0.61
5	Head	298.70	300	0.43
6	Chest	299.24	300	0.25
7	Chest	300.04	300	-0.01
8	Chest	199.60	200	0.20
9	Chest	301.10	300	-0.37
10	Chest	199.84	200	0.08
11	Pelvic	179.17	180	0.46
12	Pelvic	180.32	180	-0.18
13	Pelvic	179.65	180	0.20
14	Pelvic	179.31	180	0.38
15	Pelvic	179.52	180	0.27
Average				0.27
Standard deviation				0.29

Table 4.13 is the results performed the clinical cases in IMRT plans in head, chest and pelvic regions by calculating from Acuros XB algorithm and measuring from ionization chamber in CIRS inhomogeneous phantom. The average dose difference in IMRT was -0.60±1.05% with the error range from -2.27% to 0.53% that were higher than in 3D-CRT and VMAT techniques. It was because IMRT plan was more complicated plan and the chamber position may be located in the high dose gradient region. However, the errors from all the test cases were still within ±5.00% limitation defined by ICRU Report No 40.

Table 4.13 The dose difference between measurement and calculation in the CIRS phantom as the inhomogeneous medium for IMRT technique.

Case No.	Regions	Measurement (cGy)	Calculation (cGy)	Difference (%)
1	Head	300.51	300	-0.17
2	Head	199.43	200	0.29
3	Head	200.18	200	-0.09
4	Head	200.18	200	-0.09
5	Head	200.45	200	-0.22
6	Chest	204.18	200	-1.42
7	Chest	202.88	200	0.10
8	Chest	199.80	200	-2.27
9	Chest	204.64	200	0.25
10	Chest	199.51	200	-1.42
11	Pelvic	180.04	180	-0.02
12	Pelvic	198.95	200	0.53
13	Pelvic	234.93	230	-2.10
14	Pelvic	228.73	224	-2.07
15	Pelvic	199.22	200	0.39
Average				**-0.60**
Standard deviation				**1.05**

Table 4.14 displays the results of VMAT plans in head, chest and pelvic regions by calculating from Acuros XB algorithm and measuring from ionization chamber in CIRS inhomogeneous phantom. The average dose difference in VMAT was -1.12±0.44% with the error range from –1.90% to -0.34% that were lower than in IMRT technique. However, the errors from all the test cases were still within ±5.00% limitation defined by ICRU Report No 40.

Table 4.14 The dose difference between measurement and calculation in the CIRS phantom as the inhomogeneous medium for VMAT technique.

Case No.	Regions	Measurement (cGy)	Calculation (cGy)	Difference (%)
1	Head	222.08	220	-0.94
2	Head	182.53	180	-1.39
3	Head	202.19	200	-1.08
4	Head	181.53	180	-0.85
5	Head	203.88	200	-1.90
6	Chest	121.38	120	-1.14
7	Chest	303.45	300	-1.14
8	Chest	203.39	200	-1.67
9	Chest	200.68	200	-0.34
10	Chest	203.56	200	-1.75
11	Pelvic	302.65	300	-0.87
12	Pelvic	182.04	180	-1.12
13	Pelvic	204.71	202.5	-1.08
14	Pelvic	200.79	200	-0.39
15	Pelvic	218.46	216	-1.13
Average				**-1.12**
Standard deviation				**0.44**

CHAPTER V

CONCLUSIONS

In this study, the measurements from detector and calculations from Acuros XB algorithm were compared in two steps. The first step, the percentage depth doses, beam profiles and output factors were measured and calculated in homogenous (water phantom). The second step, the clinical applications of 3D-CRT, IMRT and VMAT plans were measured and calculated in the homogeneous (solid water phantom) and inhomogeneous (CIRS phantom) medium. Acuros XB algorithm has the potential to result in accurate and faster in dose calculation. The following are the results of calculations and measurements by Acuros XB algorithm.

1. Percentage depth dose comparisons between measurements and calculations were in a good agreement within the tolerance (2% dose difference of δ_1 and 2 mm distance to agreement of δ_2) for all field sizes.
2. Beam profile comparisons between measurements and calculations were in the acceptable criteria ($\delta_2 = 2$ mm, $\delta_1 = 3\%$ dose, $\delta_4 = 3\%$ and $\delta_{50\text{-}90} = 2$ mm), however, the deeper profile displays the higher dose differences, especially in the low dose and small gradient region.
3. The agreement of output factors between measurements and calculations showed very excellent results for all field sizes in square and rectangular fields with the difference within 2% of tolerance limits.
4. From point dose comparisons between measurements and calculations in 15 cases of 3D-CRT, IMRT and VMAT plans in different regions for homogeneous and inhomogeneous medium showed the excellent result in 3D-CRT and good agreement in IMRT and VMAT techniques.
5. The dose differences between Acuros XB algorithm calculations and measurements are within the recommendation of AAPM TG-53 and IAEA TRS 430.

Therefore, the Acuros XB algorithm can be implemented in Eclipse treatment planning system for clinical application in radiotherapy

REFERENCES

[1]. Failla, G.A., et al., "Acuros XB advanced dose calculation for the Eclipse treatment planning system". Palo Alto, CA: Varian Medical Systems, 2010.

[2]. Hoffmann, L., et al., "Clinical validation of the Acuros XB photon dose calculation algorithm, a grid-based Boltzmann equation solver". Acta oncologica, 2012. 51(3): p. 376-385.

[3]. Fraas, B., K. Doppke, and M. Hunt, "Quality assurance for clinical radiotherapy treatment planning, AAPM Radiation Therapy committee TG53". Med. Phys, 1998. 25(1773): p. 1829.

[4]. Vassiliev, O.N., et al., "Validation of a new grid-based Boltzmann equation solver for dose calculation in radiotherapy with photon beams". Physics in medicine and biology, 2010. 55(3): p. 581.

[5]. Han, T., et al., "Experimental validation of deterministic Acuros XB algorithm for IMRT and VMAT dose calculations with the Radiological Physics Center's head and neck phantom". Medical physics, 2012. 39(4): p. 2193-2202.

[6]. Golnik, N., T. Wilczynska-Kitowska, and M. Zielczynski, "Determination of the Recombination Index of Quality for Neutrons and Charged Particles Employing High Pressure Ionisation Chambers". Radiation Protection Dosimetry, 1988. 23(1-4): p. 273-276.

[7]. Andreo, P., et al., "Commissioning and quality assurance of computerized planning systems for radiation treatment of cancer". International Atomic Energy Agency technical report series, 2004(430).

[8]. HORTON, J.L., et. al., "Acceptance tests and commissioning measurements. Radiation oncology physics": A handbook for teachers and students. Vienna: International Atomic Energy Agency, 2005: p. 355-385.

[9]. 48, A.R.N., et. al., "The Calibration and Use of Plane-Parallel Ionization Chambers for Dosimetry of Electron Beams". 1994: Medical Physics.

[10]. Kartutik, K., W. Wibowo, and S. Pawiro. "Comparison of radiotherapy dosimetry for 3D-CRT, IMRT, and SBRT based on electron density calibration". in Journal of Physics: Conference Series. 2016. IOP Publishing.

[11]. Liu, H.H., T.R. Mackie, and E.C. McCullough, "Calculating output factors for photon beam radiotherapy using a convolution/superposition method based on a dual source photon beam model". Medical physics, 1997. 24(12): p. 1975-1985.

[12]. Gupta, T., et al., "Three-dimensional conformal radiotherapy (3D-CRT) versus intensity modulated radiation therapy (IMRT) in squamous cell carcinoma of the head and neck": a randomized controlled trial. Radiotherapy and Oncology, 2012. 104(3): p. 343-348.

[13]. Ben-Josef, E., et al., "Intensity-modulated radiotherapy (IMRT) and concurrent capecitabine for pancreatic cancer". International Journal of Radiation Oncology, Biology Physics, 2004. 59(2): p. 454-459.

[14]. Breitman, K., et al., "Experimental validation of the Eclipse AAA algorithm". Journal of Applied Clinical Medical Physics, 2007. 8(2).

[15]. Rana, S., et al., "Acuros XB Algorithm vs. Anisotropic Analytical Algorithm: A Dosimetric Study Using Heterogeneous Phantom and Computed Tomography (CT) Data Sets of Esophageal Cancer Patients". 2013.

[16]. Verbakel, W.F., et al., "Volumetric intensity-modulated arc therapy vs. conventional IMRT in head-and-neck cancer: a comparative planning and dosimetric study". International Journal of Radiation Oncology Biology Physics, 2009. 74(1): p. 252-259.

[17]. Podgorsak, E., Radiation oncology physics. "a handbook for teachers and students/EB Podgorsak".Vienna: International Atomic Energy Agency, 2005. 657.

[18]. Aragón-Martínez, N., et al., "Characterization of radiation beams used to determinate the correction factor for a CyberKnife® unit reference field using ionization chambers". in AIP Conference Proceedings. 2014. AIP.

[19]. Muir, B., et. al., "Ion chamber absorbed dose calibration coefficients", ND, w, measured at ADCLs: Distribution analysis and stability. Medical physics, 2015. 42(4): p. 1546-1554.

[20]. Rikner, G. and E. Grusell, "General specifications for silicon semiconductors for use in radiation dosimetry". Physics in Medicine and Biology, 1987. 32(9): p. 1109.

[21]. Greene, D. and P.C. Williams, "Linear accelerators for radiation therapy". 1997: CRC Press.

[22]. Cattaneo, G.M., et al., "Treatment planning comparison between conformal radiotherapy and helical tomotherapy in the case of locally advanced-stage NSCLC". Radiotherapy and oncology, 2008. 88(3): p. 310-318.

[23]. Grosswendt, B., et. al., "Dependence of the photon backscatter factor for water on source-to-phantom distance and irradiation field size". Physics in Medicine and Biology, 1990. 35(9): p. 1233.

[24]. Attix FH, P.B. "A solid water phantom material for radiotherapy x-ray and gamma-ray beam calibrations". 1982 [cited 2016.

[25]. Followill, D.S., et al., "Design, development, and implementation of the radiological physics center's pelvis and thorax anthropomorphic quality assurance phantoms". Medical physics, 2007. 34(6): p. 2070-2076.

[26]. McEwen, M.R., et. al., "Measurement of ionization chamber absorbed dose kQ factors in megavoltage photon beams". Medical physics, 2010. 37(5): p. 2179-2193.

[27]. FC65-P, F.T.C. "FC65-P ""Farmer"" type ion chamber: 0.65 ccm, POM, waterproof, TNC triax". 2009.

[28]. 3G, I.P. "IBA PFD 3G Photon Dosimetry Diode Detector - Radiation Products". [cited 2016.

[29]. Dosimetry, D.I. "High Performance Reference Class Electrometer". [cited 2016.

[30]. Fornell, C., et. al., "A national customer satisfaction barometer": The Swedish experience. the Journal of Marketing, 1992: p. 6-21.

[31]. Yaron, M., S.R. Lowenstein, and J. Koziol-McLain, "Measuring the accuracy of the infrared tympanic thermometer": correlation does not signify agreement. The Journal of emergency medicine, 1995. 13(5): p. 617-621.

APPENDIX

VITA

Name: Mr. Yot Phimmakone

Sex: Male

Nationality: Lao

Date of birth: October 10, 1990

Place of birth: Xiengkhouang Province, Laos

Institutions Attended: The National University of Laos,

                               2014 Bachelor of Science (General Physic)

Home Address: Mittaphab Hospital, Vientiane, Laos

Email: yotphimmakone@gmail.com